POLITECNICO DI TORINO

Master's Degree Course in Aerospace Engineering

Master's Degree Thesis

A space-borne Doppler radar end-to-end simulator for the ESA WIVERN mission

Supervisors
Prof. Alessandro Battaglia
Prof. Fabrizio Stesina

Candidate
Paolo Martire

October 2021

Ai familiari e agli amici
che mi hanno sostenuto
in questi anni.
Questo traguardo è
anche merito vostro.

"To me, it underscores our responsibility to deal more kindly with one another, and to preserve and cherish the pale blue dot, the only home we've ever known." – *Carl Sagan*

Abstract

In June 2021, the WIVERN (WInd VElocity Radar Nephoscope) mission has been selected to enter Phase 0 studies in the context of the 11th call of the ESA Earth Explorer program. The mission will provide novel observations of global winds, clouds and precipitation by a ground-breaking conically scanning dual-polarization Doppler W-band (94-GHz) radar.

End-to-End (E2E) simulators represent critical tools to assess in-flight performances and support the consolidation of mission architecture and payload design and are essential during Phase 0 ESA studies and beyond. This dissertation describes the original work carried out to develop an E2E radar simulator tailored to the WIVERN mission, showcasing its capabilities for a case study of interest.

The simulator reproduces WIVERN observations by simulating the satellite orbiting around the Earth in a polar Sun-synchronous orbit and looking down at an atmosphere described by a global circulation model that provides fine resolution vertical profiles of winds and clouds. The simulator implements the orbital model, the scanning geometry and the different polarization modes of the radar, thus identifying the volume sampled by the radar over time. The radar sampled volume is then linked to the output of the global cloud model to derive the Level 2a products of the mission, i.e. measured reflectivities and Doppler velocities of the atmospheric targets. The simulator also addresses specific issues affecting the radar measurements: surface clutter, effects of cross-polarization, nonuniform beam filling and mispointing errors.

Given its modular structure, the simulator allows the easy investigation of different orbits, scanning geometries and radar layouts, thus enabling comparisons among a variety of configurations. In the set-up currently proposed for the Earth Explorer 11, results based on a single global model output simulation demonstrate that the science requirements for the mission (accuracy of the line of sight winds of less than 1.4 m/s) can be achieved.

Table of Contents

List of Tables

List of Figures

Acronyms

CoM

Center of Mass

E2E

End-to-End

IFFT

Inverse Fast Fourier Transform

LDR

Linear Depolarization Ratio

LOS

Line of sight

NRCS

Normalized Radar Cross-Section

NUBF

Non-Uniform Beam Filling

NWP

Numerical Weather Prediction

PIA

Path-Integrated Attenuation

PRF

Pulse Repetition Frequency

PRI

Pulse Repetition Interval

PSD

Power Spectral Density

RAAN

Right Ascension of the Ascending Node

SGR

Signal-to-Ghost Ratio

SNR

Signal-to-Noise Ratio

SSO

Sun-Synchronous Orbit

WMO

World Meteorological Organization

Chapter 1

The Wivern mission

Tropical cyclones, windstorms and other weather extremes have been representing a increasing threat over the years. Everyone is familiar with the magnitude and scale that such severe weather phenomena can reach and the enormous damage they leave past them. Life losses and billions-worth economic damages have tragically drawn attention to weather hazards, such that the World Meteorological Organization (WMO) identifies preparedness towards hydrometeorological extremes as one of its top priorities [21]. It is thus essential to improve the accuracy of weather forecasting, allowing an earlier and more effective response wherever these events may occur. [16]

1.1 Context

Global profile measurements of three-dimensional winds would be a significant step forward in improving initial conditions for weather forecasts models, thus enhancing weather prediction skills. The lack of winds data indeed represents a deficit in the observing system and limits further advances in weather predictions. [4][16]

Currently, different types of winds observations are carried out. Land stations, ships and buoys can take measurements at the surface, while airplanes, flying on traditional air routes, measure winds at cruising altitude and during ascent and descent phases (thus obtaining, in the latter case, vertical profiles near airports). Typically, vertical observations mainly come from wind profiling radars and radiosoundings. In the latter case, a radiosonde on a weather balloon takes measurements of the atmospheric quantities of interest during the ascent and transmits them to a ground station. These observations are carried out chiefly by weather stations located in the Northern Hemisphere, so only a number of discrete vertical profiles is taken. Lastly, there are observations from space. Winds can indeed be derived from the time evolution of geostationary satellites imagery, but these estimates concern only the clouds' tops and don't carry a precise information about their altitude. Additional measurements from scatterometers on satellites derive winds at the surface from sea roughness. In summary, global coverage of winds profiles is hardly possible with the above methods, so new observation techniques, primarily from space, have been developed. [4]

In 2018 the European Space Agency (ESA) launched the mission Aeolus, which provides wind profile observations by using, for the first time, a space-based Doppler wind lidar. Moving in a Sun-synchronous orbit, with a 90° angle to the satellite track and an off-nadir angle of 35°, the lidar can detect the horizontal components of winds (mostly east-west) by measuring the line-of-sight velocities in the clear sky. The Aeolus mission responds to the need to collect more wind profiles for the WMO Global Observing System, used globally for weather forecast models. Since Aeolus measurements were adopted, several weather centers worldwide, including the European Centre for Medium-Range Weather Forecasts (ECMWF), have experienced a significant improvement in weather forecasting. [2]

Following ESA's call for the 11th Earth Explorer, the newly proposed **WIVERN** (WInd VElocity Radar Nephoscope) mission will provide additional wind measurements that will complement Aeolus observations. The Wivern W-band radar can indeed measure winds within optically thick clouds, where the lidar sensor cannot see. The combination of these measurements will then allow the detection of the wind fields with global coverage. [17]

Earth Explorer program Both Aeolus and Wivern missions fit within the ESA's Earth Explorer program. The Earth Explorers are research missions aiming to resolve the scientific issues highlighted by the Earth science community while serving as a technology demonstrator for groundbreaking observation techniques. Aeolus has been selected as the 5th Earth Explorer, while Wivern is competing for the 11th Earth Explorer program. In June 2021, after a first selection, Wivern and three other missions (Cairt, Nitrosat and Seastar) have been selected to proceed with pre-feasibility studies. Further down-selections are planned in 2023 and 2025, with the intent to launch the future Earth Explorer-11 mission in 2031-2032 [1][3].

1.2 Mission description

The Wivern mission idea responds to the need to advance the actual observation capabilities of winds, clouds and precipitation. To meet its core objectives, Wivern builds around the concept illustrated in figure (1.1): a conically scanning dual-polarization Doppler radar will measure line-of-sight winds and reflectivity profiles, tracing out an 800 km wide swath while moving on a Sun-synchronous orbit. In detail, the mission will address the following science objectives [**SO**]:

1. **[SO1]**: "*to extend the lead time of useful prediction skills of hazardous weather (e.g., wind-storm, cyclones, floods) by direct assimilation of wide-swath winds from clouds and profiles of radar reflectivity of clouds and precipitation into numerical weather prediction (NWP) models.*"

2. **[SO2]**: "*to improve numerical models by providing new metrics and observational verification to assess different NWP parameterisation schemes within such models. NWP and climate models use similar schemes so better NWP models will also augment confidence in climate models.*"

3. **[SO3]**: "*to establish a benchmark for the climate record of cloud profiles, global solid/light precipitation, and, innovatively, winds, crucial for a better quantification of the Earth's hydrological cycle, and energy budgets, with a significant reduction in sampling errors of current and planned cloud radar missions.*" [17]

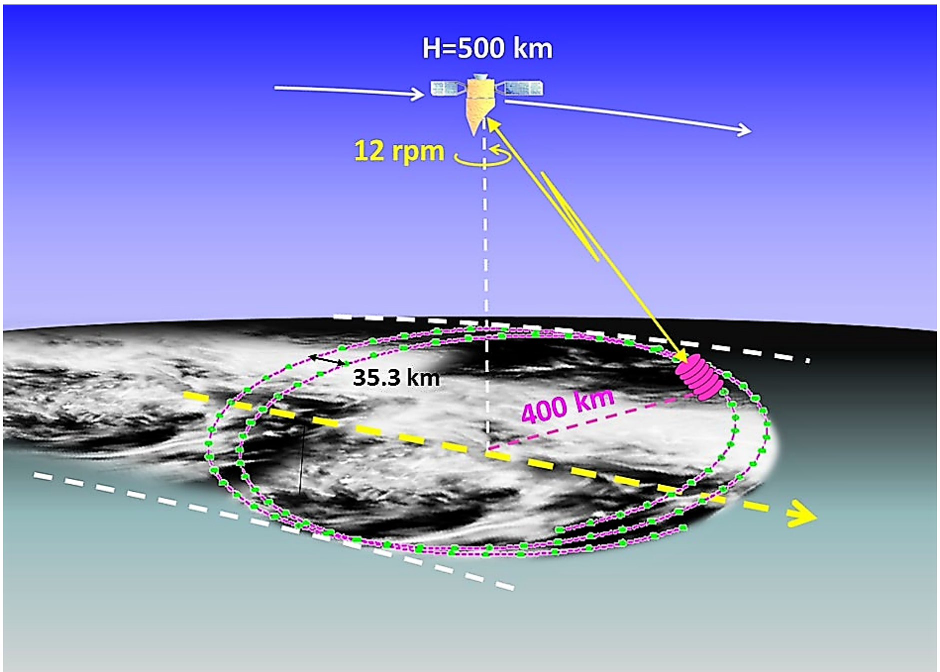

Figure 1.1: The WIVERN concept: a 94-GHz Doppler radar with 3-m antenna scanning at 12 RPM tracing out a cycloidal track with an incidence angle of 41.6°. [17]

As outlined in the science requirements, Wivern will provide in-clouds reflectivity and line-of-sight winds data for the assimilation into global NWP models. For the data assimilation of winds profiles, the main observables of the mission, the WMO has set the requirements listed in table (1.1). First of all, it should be noted that these requirements refer to the horizontal winds, whereas Wivern will detect the ones along its line of sight. If the terminal velocity of hydrometeors is known and the vertical component of the wind is negligible, from LOS measurements is possible to derive the horizontal wind component along the horizontally-projected line of sight (HLOS). Wivern is expected to provide between 1-2 million HLOS winds per day with 2 m/s precision for targets with reflectivities above -15 dBZ. Reaching this accuracy requires collecting and averaging the measurements taken over a total distance of 20 km along the scan ground track. Accordingly, the horizontal resolution of the winds will be 20 km, as reported in table (1.1). The radar is sounding the atmosphere down to the ground with a range resolution of 500 m. Figure (1.2) illustrates the observing slant geometry; the actual vertical resolution will be the result of the range resolution, the antenna beamwidth and the satellite altitude [20]. Note that, for a uniform cloud, 90% (99%) of the backscattering power is coming from a region whose vertical extent is 640 m (980 m). The horizontal sampling pattern is a function of the rotation speed. The values used here (table 1.1) are the result of a preliminary optimization for wind product performance (sensitivity and spatial resolution).

Table 1.1: WMO (World Meteorological Organization) requirements for horizontal winds for numerical weather prediction (NWP) and the expected performances of WIVERN. [17]

	Uncertainty	Horizontal Resolution	Vertical Resolution	Observing Cycle
Goal	2 m/s	15 km	0.5 km	1 hr
Breakthrough	3 m/s	100 km	1 km	6 hr
Threshold	5 m/s	100 km	3 km	12 hr
WIVERN	2 m/s	20 km	0.64 km	1 to 1.5 days

In summary, Wivern should be able to meet the accuracy goal and the horizontal and vertical resolution breakthrough objectives for in-cloud winds. On the other hand, the observing cycle requirements are challenging and would require a satellite constellation. Industrial studies show that for the selected SSO and scan geometry Wivern displays an average revisit time of 1.5 days in the Tropical band and 1 day or less for latitudes above 50° and below $-50°$. [16][17]

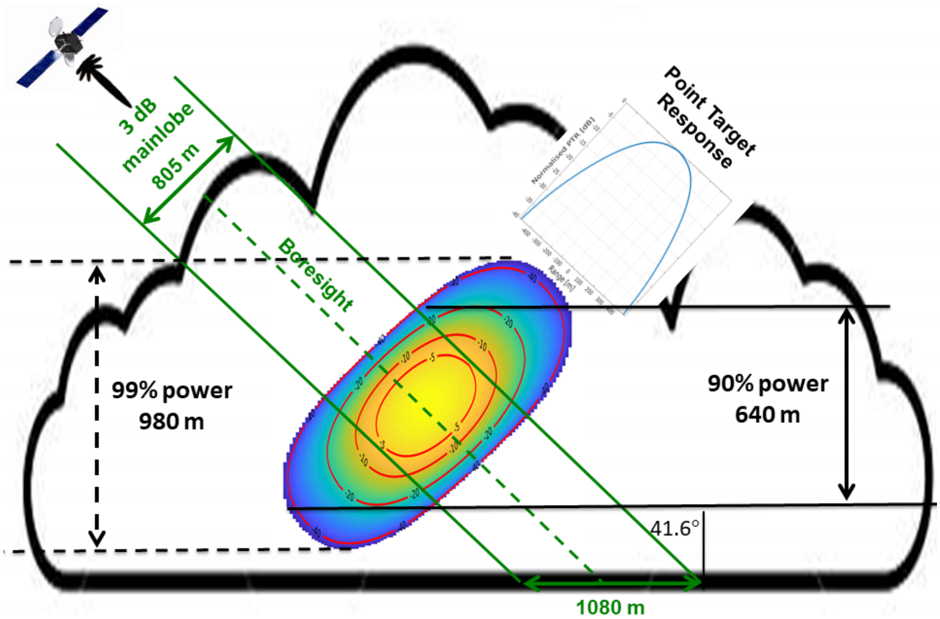

Figure 1.2: Schematic illustrating the WIVERN observing geometry. The specifics of the radar are detailed in table (1.3). [17]

Table 1.2: Specifics of the satellite orbit as proposed in a recent ESA Earth Explorer 11 call. [17]

Orbit element	Symbol	Mean	Osculating	Unit
Semi-major axis	a	6878.000	6887.4534	km
Eccentricity	e	0.001257	0.00135062	
Inclination	i	97.418	97.4011	deg
RAAN	Ω	-169.387	-169.6234	deg
Argument of perigee	ω	90.0	69.4689	deg
Mean Anomaly @ t_0	M	0	-69.2253	deg
Mean LTAN		6.000	-	hour
Epoch t_0		2019-01-01 06:00:00		
Reference Frame		J2000		

Table 1.3: Specifics of the radar for the simulation. The configuration here adopted is the one proposed for WIVERN in a recent ESA Earth Explorer 11 call. The E2E simulator can study various trade-offs to optimise mission, system and instrument parameters. [17]

Satellite altitude, h_{sc}	500	km
Satellite velocity, v_{sc}	7600	m/s
Off-nadir pointing angle	38	deg
Incidence angle	41.6	deg
RF output frequency	94.05	GHz
Pulse width	3.3	μs
Antenna beamwidth, ψ_{3dB}	0.071	deg
Circular antenna diameter	3	m
Rotation speed	12	rpm
Footprint speed	500	km/s
Transmit polarization	H or V	
Cross-polarization	< -25	dB
Single pulse sensitivity	-18	dBZ
H-V Pair Repetition Frequency	4	kHz
Range sampling distance (rate)	100 m (1.5 MHz)	
Number of H-V Pairs per 1 km integration length	8	

Chapter 2

Theory

2.1 Weather radar basic principles

Information about an object can be collected through *in-situ* sensing, in which the sensor is in direct contact with the object, or through *remote* sensing, in which the information must travel between the object and the sensor. Remote sensors can be defined as *passive* or *active*: passive remote sensors collect energy radiated or reflected off the object by some other radiation sources, while active remote sensors provide illumination to the target. A well-known active remote sensor is the RADAR (RAdio Detection And Ranging), an instrument that emits a signal at microwave or radio frequencies and then listens for echoes occurring if the EM wave reflects off objects placed along its path. Because an energy source is needed to transmit the signal, active remote sensors such as radars are generally more complex than passive remote sensors. However, since the time of transmission and signal properties are known, the echo can be compared to the transmitted signal. In particular, it is possible to measure the time elapsed between transmission and reception, compare the strength of the received signal to the transmitted one and detect changes in frequency and polarization. These measurements allow to gather additional information about the size, composition and distance of the object, but also about the medium in which the signal travels. [15]
A weather radar system works as set out below:

1. The transmitter generates a high-power pulse characterized by a typical duration τ of few µs. The pulse passes through a hollow metal tubing known as a waveguide that directs the signal towards a circulator, whose task is to send the transmitter power towards the antenna and the returns from targets towards the receiver circuitry.

2. When considering a reflector antenna, the wave is directed by a feed towards the reflector and then scattered into multiple waves that can either interfere

constructively or destructively. At a sufficient distance from the antenna, the waves interfere constructively along the boresight direction while canceling partially or completely each other where destructive interference happens. The corresponding beam pattern has several sidelobes pointing in all directions and a main lobe with a half-power beamwidth (in radians) of:

$$\psi_{3dB} \approx 1.22 \frac{\lambda}{D_a} \tag{2.1}$$

where D_a is the diameter of the parabolic reflector and λ is the wavelength. When ignoring the sidelobes, a typical approximation consists in assuming a Gaussian antenna pattern, with the squared antenna gain being:

$$G^2(\psi) = G_0^2 \exp\left[-8\log(2)\left(\frac{\psi}{\psi_{3\mathrm{dB}}}\right)^2\right] \equiv G_0^2 f_a^2(\psi) \tag{2.2}$$

where G_0 is the antenna gain in the boresight direction and ψ is the polar angle with respect to the boresight.

3. The pulse transmitted by the antenna propagates as an expanding shell of thickness $c\tau/n$ that moves with speed c/n, where c is the speed of light in vacuum and n is the refractive index of the medium (assumed to be 1 from this point on). After firing a pulse, the transmitter becomes silent to allow the receiver to detect the tiny fraction of the transmitted energy backscattered to the radar. The reflector focuses the received signal into the feed and the waveguide, and then the circulator directs it toward the receiver circuitry.

4. Finally, the signal processors extract data from the received signal, while the radar product generator process these data to obtain meteorological information. [15]

Weather radars operate within a defined range of wavelengths, spanning from meters (shorter radio waves) down to few millimeters (microwaves region). The employed frequencies belong to the portions of the EM spectrum, known as atmospheric windows (see figure (2.1)), to which the atmosphere is transparent. Moreover, radio waves and longer microwaves can also pass through clouds and storms without being affected by excessive attenuation, thus justifying the radar's ability to monitor weather phenomena.

While traveling through the atmosphere, the EM waves can encounter objects or particles that re-emits a portion of the incident radiation in a process known as scattering. Different scattering regimes exist, depending on the radiation wavelength λ and the scatterer size. When the scatterer size is smaller than λ, the Rayleigh scattering occurs. In this regime, the fraction of scattered irradiance is proportional

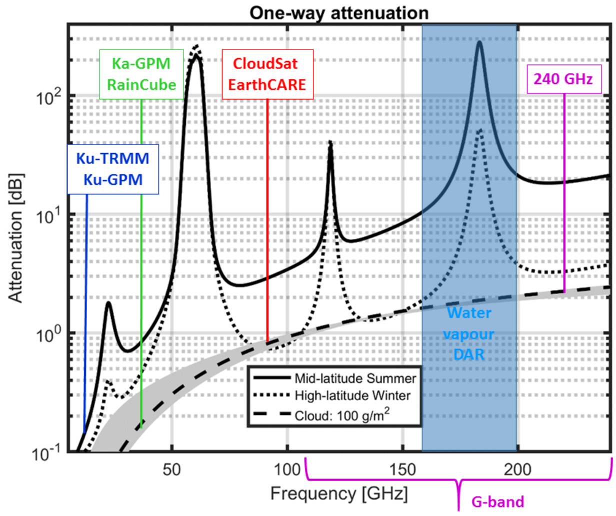

Figure 2.1: Gas attenuation in the range of frequencies between 5 and 250 GHz for two types of atmospheres (a very moist, mid-latitude summer atmosphere and a very dry, high-latitude winter atmosphere). Attenuation due to cloud water at 10°C for a total of 100 g/m^2 is plotted in dashed line with the gray shading corresponding to the variability when moving temperature from -35°C to $+30$°C. Radar frequencies are generally selected in the window regions, that is, away from the water vapor and the oxygen absorption bands, apart for the differential absorption radar with frequency located in the 183 GHz water vapor absorption band (blue shaded region). WIVERN will be operated at W-band. Extracted from [11].

to D^6/λ^4, being D the diameter of the scatterer, assumed to be spherical. This relation suggests that at fixed λ, larger targets scatter considerably more than smaller ones and that, given a scatterer of diameter D, the scattering increases significantly as the radiation wavelength decreases. The latter observation also means that smaller scatterers are easier to detect for radars employing shorter wavelengths. [15]

2.2 Pulsed Doppler weather radars

A pulsed radar emits short bursts of electromagnetic energy of duration τ, separated from one another by a time interval known as Pulse Repetition Interval (PRI). The inverse of the PRI defines the number of pulses emitted per second and it is called the Pulse Repetition Frequency (PRF). Knowing the initial time t_0 at which the pulse transmission starts and recording the time of arrival of the echo coming from the i-th target, the radar can derive the targets range as follows:

$$r_i = \frac{c(t_i - t_0)}{2} \tag{2.3}$$

where the factor 2 in the denominator accounts for the signal traveling back and forth to the target. Some echos coming from distant targets can reach the antenna after the second or subsequent pulse is fired, generating range ambiguities. The radar indeed cannot distinguish between an echo from a closer target generated by the last fired pulse and one arriving from a greater distance, but originating from a previous pulse. This range ambiguity is avoided if all the targets generate echoes within a time shorter than the pulse repetition interval PRI, or equivalently when their range is within the radius:

$$r_{\max} = \frac{c\,\mathrm{PRI}}{2} \tag{2.4}$$

also known as the *maximum unambiguous range* [5].[15]

Besides determining their distances, the radar should also be able to detect two o more close targets as distinct ones. The minimum range down to which the radar can do this identifies its range resolution, defined as:

$$\Delta r = \frac{c\tau}{2} \tag{2.5}$$

If two targets ranges differ less than Δr, the echo of the farther object partially overlaps with the returns of the closer one, thus mistakenly leading the radar to perceive two separate targets as a distributed one [5]. In this case, the round-trip distance between the objects is inferior to $c\tau$, so the echo of the farthest target reaches the closer one while still being illuminated by the pulse. Weather radars typically deal with distributed targets composed of billions of scatterers at very close distances, so given that this uncertainty exists, the measurement of a quantity at a range r also includes the contributions of the nearby scatterers placed at different ranges. Consequently, the values of a quantity associated with a range r will be averaged over a *backscattering volume* $\mathcal{V}$, defined as the intersection between a cone with an opening angle $\psi_{3\mathrm{dB}}$, and a spherical shell with an inner radius of $r - \Delta r/2$ and an outer radius of $r + \Delta r/2$.

2.2.1 Doppler principle

In the transmission phase, the radar generates a signal in the form of $s_0(t) = A\sin(\omega_0 t + \phi)$, being A the amplitude, ω_0 the transmission angular frequency and ϕ the phase constant. When a single target at range r scatters part of the incident radiation back to the radar (assuming no phase change upon scattering), if no relative velocity subsists, the echo at the radar will be in the form of:

$$s(r,t) = B \sin\left[\omega_0 \left(t - \frac{2r}{c}\right) + \phi\right] \tag{2.6}$$

where the term $-\omega_0(2r/c)$, denoted by φ, is called the *phase shift* and accounts for the wave motion over the distance $2r$. If a relative motion exists between the radar and the target, the phase of equation (2.6) will change in time, so its time derivative is:

$$\omega = \frac{d}{dt}\left[\omega_0 \left(t - \frac{2r}{c}\right) + \phi\right] = \omega_0 - \omega_0 \frac{2\dot{r}}{c} \tag{2.7}$$

hence the angular frequency ω detected at the receiver increases if $\dot{r} < 0$ and decreases when $\dot{r} > 0$. This is known as the *Doppler effect*, which formally should be treated as a relativistic effect, but since the velocities involved (few km/s) are still far lower than c, then a non-relativistic approach is a completely valid approximation. The signal at the receiver will then be:

$$s(r,t) = C \sin\left[\omega \left(t - \frac{2r}{c}\right) + \phi\right] \tag{2.8}$$

From equation (2.7), recalling that $\omega_0 = 2\pi f_0 = 2\pi c/\lambda_0$ and introducing the radial velocity $v_r = \dot{r}$, the difference between the angular frequencies in reception and transmission is:

$$\omega_d = \omega - \omega_0 = \frac{d\varphi}{dt} = -\frac{4\pi v_r}{\lambda_0} \tag{2.9}$$

with:

$$f_d = \frac{\omega_d}{2\pi} = -\frac{2v_r}{c} f_0 \tag{2.10}$$

defined as the *Doppler shift frequency.*

Equation (2.9) can be now written in the context of a pulse radar that emits signals at frequency equal to the PRF. Within two pulses separated in time by the PRI, the relative distance between the radar and the target may change of Δd, so equation (2.9) becomes:

$$\frac{\Delta\varphi}{\mathrm{PRI}} = -\frac{4\pi v_r}{\lambda_0}$$

being $v_r = \Delta d/\mathrm{PRI}$ the Doppler velocity. The last relation may be also written as:

$$\Delta\varphi = -\frac{4\pi}{\lambda_0} \frac{v_r}{\mathrm{PRF}} \tag{2.11}$$

The term $\Delta\varphi$ represents the phase shift variation between two consecutive returns and can only assume, by definition, values in the interval $[-\pi,\, \pi[$. As a consequence, the Doppler velocity can be only measured unambiguously within $[-v_{r\,\max}, v_{r\,\max}[$, being:

$$v_{r\,\max} = \frac{\lambda_0}{4}\mathrm{PRF} \tag{2.12}$$

the Doppler velocity related to $\Delta\varphi = -\pi$, known as the *Nyquist velocity.* The constraints on v_r imply that speeds exceeding the limits will be incorrectly reported in the interval $[-v_{r\,\max}, v_{r\,\max}[$ in a phenomenon known as *velocity aliasing.* For example, by looking at equation (2.11), a target rapidly approaching the radar ($v_r < 0$) and resulting in $\Delta\varphi = \pi + \xi$ (being $0 < \xi < \pi$ a generic angle) will be mistakenly reported as one generating $\Delta\varphi = -\pi + \xi$, and so as a slower target moving away from the radar ($v_r > 0$). [5] [15][24]

Doppler spectrum width and coherency time

The previous discussion about Doppler velocity considers only the returns from a single target, when in fact the illuminated region contains billions of scatterers animated by different speeds. By looking at the same sampling volume, the received signals from two consecutive pulses differ as a result of the changing interference between the returns of the single targets, which reshuffle in time due to the different relative motions. However, to accurately measure the Doppler velocity, the pulse-to-pulse echoes should be coherent, which means that scatterers relative motion should be small compared to the signal wavelength. Therefore it is possible to identify a *coherency time* below which the signals coherency is verified:

$$t_{\mathrm{coh}} = \frac{\lambda_0}{4\pi\sigma_v} \tag{2.13}$$

The direct consequence of this relation is that the time between two pulses, namely PRI, must be lower than t_{coh}. The coherency time depends, besides the wavelength, on the *Doppler spectrum width* σ_v, which is a quantitative measure of the velocities distribution within a given volume. [18]
For a space-borne radar with the same configuration as Wivern, the expected σ_v may be around 3-4 m/s [10][25].

Doppler dilemma

From what has been reported until now, it is possible to draw some conclusions. Equation (2.4) implies that increasing the maximum unambiguous range requires the PRF to decrease. On the other hand, as shown in equation (2.12), a reduction of the PRF leads to a lower $v_{r\,\max}$ and hence a smaller range of values in which velocities can be measured unambiguously. This inherent trade-off between $r_{\max}$ and $v_{r\,\max}$ is known as the *Doppler dilemma.* On top of this, it is also necessary to consider the constraints on PRF dictated by the coherency time (2.13), since PRI shall be less than t_{coh}. The solution to these issues is based on the introduction of polarization diversity.

2.2.2 Polarization diversity

For an electromagnetic plane wave, the electric and magnetic fields $\vec{E}$ and $\vec{B}$ are orthogonal to each other and the direction of propagation. Being the EM waves transverse waves, for them is significant the concept of polarization. Calling x the propagation direction, the electric field direction (and so the magnetic field direction, always perpendicular to $\vec{E}$) may change in function of the coordinate x and the time t following a precise law, which defines a polarized wave. The simplest case consists of an electric field always oscillating in the same plane, known as linear polarization. If the oscillation occurs in the x-y plane, the wave is horizontally polarized (H), whereas is vertically polarized (V) when $\vec{E}$ oscillates in the x-z plane.

Dual-polarization radars can transmit waves with both horizontal and vertical polarizations, often switching from pulse to pulse. Since these radars can receive signals with both polarizations, the emitted wave at H or V polarization can be measured at the opposite polarization (V and H, respectively), thus receiving a signal denoted as *cross-polar* (either HV or VH). In addition to this, the radar can emit and receive signals at the same polarization (either HH or VV), which are denoted as *copolar*. [15] [19]

Wivern dual-polarization radar configuration

As anticipated earlier, dual-polarization represents the key to resolve the Doppler dilemma and the coherency time issue, so let's see why. The coherency time defined in equation (2.13) put a strict limit on the maximum time interval between two pulses, leading to a short separation in space as well. Consequentially, successive pulses will be in the troposphere at the same time, causing the potential overlapping of their echoes if the same polarization is employed. On the contrary, two pulses fired at horizontal and vertical polarization will propagate independently through the atmosphere and therefore can be easily distinguished, as well as their echoes [10, 12, 22, 26]. Wivern employs the latter configuration, firing an H pulse first and then a second V pulse after $T_{\text{hv}} = 20\ \mu\text{s}$, which does not give targets the time to reshuffle, thereby assuring the signal phase pulse-to-pulse correlation. Moreover, this time interval also leads to a Nyquist velocity $v_{r\,\max} = 40$ m/s, large enough to measure unambiguously even the fastest winds. Ultimately, the dual-polarization resolves also the range ambiguity, because it is an issue concerning pulses with the same polarization. For the Wivern configuration depicted in figure (2.2), the pulses

H_1, H_2 and V_1, V_2 are separated in time by PRI = 1/PRF = 250 µs, which yields a maximum unambiguous range of $r_{\max} = 37.5$ km (large enough to locate in range all the targets along the slant path within the atmosphere). [16]

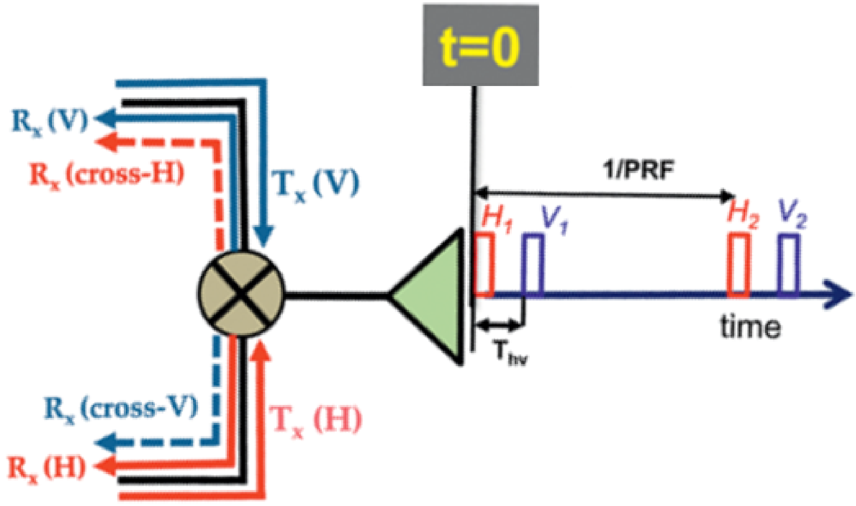

Figure 2.2: Wivern polarization diversity pulse pairs. [16]

2.3 Reflectivity

For the targets behaving as Rayleigh scatterers, it is possible to define a quantity Z known as radar reflectivity factor per unit volume:

$$Z = \int_0^\infty N(D) D^6 \, dD \tag{2.14}$$

where $N(D)$ is the number of targets of diameter D per unit volume. The linear units conventionally adopted for reflectivity are mm^6/m^3, but since its magnitude can have a great range of variation among different targets, the units generally used are decibel of mm^6/m^3, defined as:

$$Z_{\mathrm{dB}Z} = 10 \log_{10}(Z) \tag{2.15}$$

To avoid mistakes, from this point on the reflectivities appearing in formulas will have a subscript 'dBZ' when expressed in decibel units or no additional subscript when linear units are assumed.

The reflectivity can be derived by the average power $P_r(r)$ received from a given range r by using the radar equation:

$$P_r = \frac{1.22^2 0.55^2 10^{-18} \pi^7 c}{1024 \log_e(2)} \frac{P_t \tau D_a^2}{\lambda^4} \frac{T(0,r)^2}{r^2} \|K\|^2 Z \tag{2.16}$$

In which P_t is the transmitted power, τ is the pulse duration, D_a is the antenna diameter, λ is the wavelength, $T(0,r)$ is the transmittance of the medium along the signal path from range 0 to r and $\|K\|^2$ is the dielectric constant of the scatterers. Besides the assumption of parabolic antenna with a Gaussian beam pattern, the equation (2.16) is valid if the targets are spherical Rayleigh scatterers that share the same dielectric constant $\|K\|^2$. However, since there are uncertainties about the targets' nature and their behavior as Rayleigh scatterers or not, the dielectric constant is assumed to be equal to the value of the liquid water $\|K_w\|^2 = 0.93$, taken as a reference because most of the hydrometeors are in the liquid phase. Consequently, the radar equation yields a different value of reflectivity, named *measured* reflectivity Z_m. When attenuation is negligible, the obtained value is called *equivalent* reflectivity Z_e, with the two quantities linked as follows:

$$Z_{m\,\mathrm{dB}Z} = Z_{e\,\mathrm{dB}Z} - 2\,\mathrm{PIA} = Z_{e\,\mathrm{dB}Z} - 2\int_0^r k_{ext}\,ds \tag{2.17}$$

The acronym PIA stands for path-integrated attenuation and is computed as the integral of the extinction coefficient k_{ext} (dB/km) from 0 to the range r (km). The PIA measures the oneway attenuation affecting the signal while traveling towards the target at the range r. But since the backscattered signal must travel back to the radar along the same path, the total attenuation will be double, thus justifying the factor 2 in the (2.17).

LDR

When transmitting a signal at a given polarization (e.g. H), the targets may backscatter some of the radiation at the orthogonal polarization (e.g. V) other than at the same transmitting polarization. This phenomenon is called *depolarization*, and it generates the cross-polar signals HV and VH in dual-polarization radars. The ratio between a cross-polar signal (e.g. HV) and a copolar signal with the same transmitted polarization (e.g. HH) is referred to as *linear depolarization ratio* (LDR), defined as follows:

$$\mathrm{LDR}_{\mathrm{dB}} \equiv 10 \log_{10}\left(\frac{Z_{\mathrm{cx}}}{Z_{\mathrm{co}}}\right) = Z_{\mathrm{cx}\,\mathrm{dB}Z} - Z_{\mathrm{co}\,\mathrm{dB}Z} \tag{2.18}$$

where Z_{cx} and Z_{co} are the measured cross-polar and copolar reflectivities appearing in both linear and dBZ units, while the LDR is in dB units. Strictly speaking, one should define the $\mathrm{LDR_H}$ for the H channel ($Z_{\mathrm{cx}} = Z_{\mathrm{HV}}$ and $Z_{\mathrm{co}} = Z_{\mathrm{HH}}$) and the $\mathrm{LDR_V}$ for the V channel ($Z_{\mathrm{cx}} = Z_{\mathrm{VH}}$ and $Z_{\mathrm{co}} = Z_{\mathrm{VV}}$). As a first approximation, it will be assumed that $Z_{\mathrm{HV}} = Z_{\mathrm{VH}}$ and $Z_{\mathrm{HH}} = Z_{\mathrm{VV}}$, so the two LDR definitions are coincident. [15][27]

2.4 Disturbances

2.4.1 Surface clutter

While moving on its slant path, the signal will get closer to the Earth and eventually reach its surface. As a result, some echoes arriving from greater ranges can originate not only from atmospheric targets but also from the surface. These unwanted returns may corrupt or even overshadow the echoes coming from atmospheric targets and therefore are labeled as *surface clutter.*

2.4.2 Ghost echoes

A direct consequence of depolarization is the possible interference between copolar and cross-polar returning signals. The situation is depicted in figure (2.3).

At time $t = 0$, the radar starts receiving the copolar echo HH (solid red line) and the cross-polar echo HV (dashed blue line) of the first fired pulse, assumed horizontally polarized. As shown in the figure, the two profiles HV and HH are the same curve, but shifted on the y axis by an almost constant value equal to the LDR (always characterized by negative values when expressed in log units).

At time $t = 20\,\mu$s the radar also starts receiving the copolar and cross-polar echos VV and VH deriving from the second vertically polarized V pulse, fired after $T_{\mathrm{hv}} = 20\,\mu$s from the first H pulse. At this stage, the radar is receiving simultaneously two horizontally polarized signals (HH and VH) and two vertically polarized signals (HV and VV), so the returns with the same polarization may interfere, leading to a cross-talk between the two pulses. However, this is not an issue as long as the copolar signal HH (VV) is significatively stronger than the cross-polar signal VH (HV). To quantitatively compare the copolar and cross-polar signals at the same receiving polarization, the Signal-to-Ghost Ratio (SGR) is defined:

$$\begin{aligned} \mathrm{SGR_H}_{\mathrm{dB}Z}(t) &= Z_{\mathrm{HH}\,\mathrm{dB}Z}(t) - Z_{\mathrm{VH}\,\mathrm{dB}Z}(t) \\ \mathrm{SGR_V}_{\mathrm{dB}Z}(t) &= Z_{\mathrm{VV}\,\mathrm{dB}Z}(t) - Z_{\mathrm{HV}\,\mathrm{dB}Z}(t) \end{aligned} \tag{2.19}$$

The cross-talk becomes a major problem when the SGR goes below the set threshold of 3 dB, which usually happens in the presence of both large vertical reflectivity gradients and strongly depolarizing targets. The red-shaded area represents a cross-talk occurring in the atmosphere, while the blue-shaded region identifies a cross-talk due to the surface. [16]

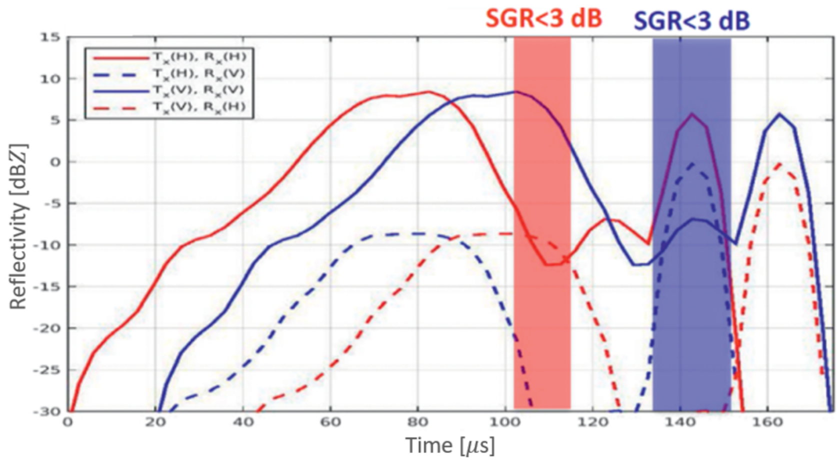

Figure 2.3: Received copolar (solid lines) and cross-polar (dashed lines) signals as function of time. The figure has a cutoff at $Z = -30$ dBZ because below this level the received echo is too weak to be detected, but in principle the curves HH and HV should start both at $t = 0$, while the profiles VV and VH at $t = 20$ μs. [16]

The time shift $T_{\rm hv}$ within a pulse pair also implies a range shift between the targets generating the copolar and cross-polar echoes arriving at the same time with the same receiving polarization. More precisely, the copolar echo of the first pulse (let's say HH) coming from a target at range r arrives at the same time with the cross-polar echo of the second pulse (VH in this case) originating from a target at range $r - cT_{\rm hv}/2$ (being the round trip distance equal to $cT_{\rm hv}$). As a consequence, the total measured reflectivity at H polarization will be:

$$Z_{\rm H}(r) = Z_{\rm HH}(r) + Z_{\rm VH}(r - cT_{\rm hv}/2) \tag{2.20}$$

On the contrary, the copolar echo of the second pulse (VV) coming from a target at the range r arrives at the same time with the cross-polar echo of the first pulse (HV) originating from a target at $r + cT_{\rm hv}/2$, so the total measured reflectivity in the V channel will be:

$$Z_{\rm V}(r) = Z_{\rm VV}(r) + Z_{\rm HV}(r + cT_{\rm hv}/2) \tag{2.21}$$

2.4.3 Noise on Doppler velocity

Uncertainties on Doppler velocity estimates depends on the Doppler spectrum width σ_v, the Signal-to-Noise (SNR) ratio, the cross-polarization interference and the number of averaged samples M. An estimate of the variance of the mean Doppler velocity can be written as [22]:

$$\mathrm{var}_{\hat{v}_D} = \frac{1}{\mathrm{M}} \frac{v_{r\,\max}^2}{2\pi^2\beta^2} \Bigg[\left(1 + \frac{1}{\mathrm{SNR}}\right)^2 + \frac{1}{\mathrm{SGR}_1} + \frac{1}{\mathrm{SGR}_2} + \frac{1}{\mathrm{SGR}_1 \mathrm{SGR}_2} \dots \\ \dots + \frac{1}{\mathrm{SNR}(\mathrm{SGR}_1 + \mathrm{SGR}_2)} - \beta^2 \Bigg] \tag{2.22}$$

where:

$$\beta \equiv \exp\left(-\frac{4\pi^2 \sigma_v^2\, T_{\mathrm{hv}}^2}{\lambda^2}\right)$$

The SNR in linear units is given by:

$$\mathrm{SNR}(r) = \frac{Z_{\mathrm{co}}(r)}{Z_{\mathrm{N}}}$$

being Z_{N} the representation in linear units of the noise level $Z_{\mathrm{N}\,\mathrm{dB}Z} = -18$ dBZ. Assuming $Z_{\mathrm{HH}} = Z_{\mathrm{VV}} = Z_{\mathrm{co}}$ and $Z_{\mathrm{HV}} = Z_{\mathrm{VH}} = Z_{\mathrm{cx}}$, the Signal-to-Ghost ratios are:

$$\mathrm{SGR}_1(r) = \frac{Z_{\mathrm{co}}(r)}{Z_{\mathrm{cx}}(r - cT_{\mathrm{hv}}/2)}$$
$$\mathrm{SGR}_2(r) = \frac{Z_{\mathrm{co}}(r)}{Z_{\mathrm{cx}}(r + cT_{\mathrm{hv}}/2)}$$

2.4.4 Mispointing

For accurate winds the pointing knowledge of the radar beam formed by the antenna must be known to at least 140 μrad (equivalent to a 1.0 m/s LOS wind uncertainty). Studies conducted by industry show that a knowledge better than 40 µrad can be obtained so that pointing errors are expected to contribute only marginally to the error budget. [17]

2.4.5 Non-uniform beam filling

Considering that Wivern makes Doppler measurements with a slant geometry from a satellite moving at 7.6 km/s, it will also detect a radial component of this velocity (a few km/s) [25]. In particular, echoes can originate from targets placed on distinct lines of sight within the backscattering volumes, leading the radar to detect different radial components of the satellite velocity. Since the platform contribution is compensated for by removing the satellite velocity along the boresight direction, a residual shear will be present within the backscattering volume (blue and red arrows in figure (2.4)). In principle, the averaging over the backscattering volume would lead to a compensation of these components, but since they are weighted by reflectivities, non-uniformities of the latter cause a not perfect compensation resulting in a velocity bias. The effect is expected to be a function of the pointing direction of the antenna relative to the satellite velocity. [7]

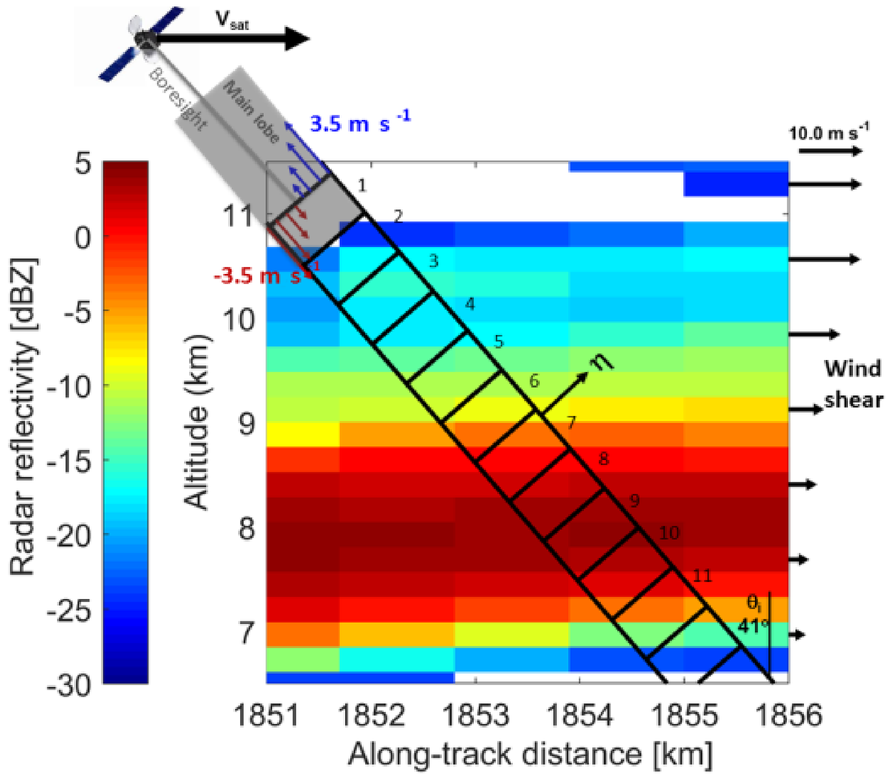

Figure 2.4: Diagram explaining Doppler velocity errors introduced by NUBF. The black rectangles represent the backscattering volumes associated with the 3 dB antenna main lobe. [7]

Chapter 3

Wivern doppler radar End-to-End simulator

This chapter describes in detail the methods employed to develop the Wivern E2E simulator. The first sections illustrate the implementation of the orbital model and

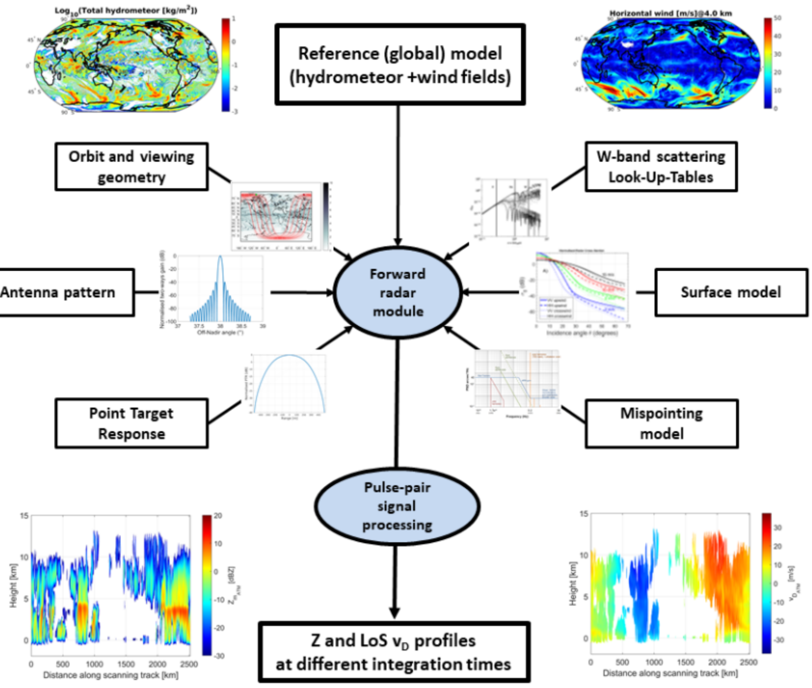

Figure 3.1: Schematic of the end-to-end simulator framework [17].

the scanning geometry, followed by a geometrical characterization of the illuminated portion of the atmosphere and the surface, which define the sampling volume over time. The sections to follow report how this sampled volume is linked to the output of the global cloud model to derive the Level 2a products of the mission (i.e., measured reflectivities and Doppler velocities of the atmospheric targets). At last, the final sections will provide a characterization of the disturbances and errors affecting the measurements.

3.1 Orbit

The E2E simulator begins with orbit propagation over a chosen time span. The orbit characteristics have been already defined by studies carried out for the Wivern proposal, so they represent an input for the Wivern simulator. Using as starting parameters the elements of table (1.2) and defining a time discretization, it is possible to propagate the orbit obtaining for each time t the spacecraft position $\vec{r}_{sc_{pqw}}(t)$ and the spacecraft velocity $\vec{v}_{sc_{pqw}}(t)$ expressed in the perifocal frame $\{O, \hat{\mathbf{p}}, \hat{\mathbf{q}}, \hat{\mathbf{w}}\}$ (see figure (3.2)), being O the Earth CoM. These vectors can also be expressed with respect to the geocentric equatorial frame[1] $\{O, \hat{\mathbf{I}}, \hat{\mathbf{J}}, \hat{\mathbf{K}}\}$ by a coordinates transformation:

$$\vec{r}_{sc_{IJK}} = \mathbf{L}_{PI}\vec{r}_{sc_{pqw}} \tag{3.1}$$

where $\mathbf{L}_{PI} = \mathbf{L}_3(\Omega(t))\mathbf{L}_1(i)\mathbf{L}_3(\omega(t))$ is the transformation matrix between the two reference frames.
As can be seen by $\mathbf{L}_{PI}$ definition, Ω and ω are assumed time-varying, while the inclination i is treated as a constant. The variation of Ω over time should be taken into account because the Wivern orbit is Sun-synchronous, and by definition this type of orbit exploits the variation of the Right Ascension of the Ascending Node (RAAN) caused by Earth's oblateness to maintain a constant angle between the orbital plane and the radial from the Sun. To do so, the orbital plane must rotate in inertial space with the same angular velocity of the Earth in its orbit around the Sun, which is 0.9856° per day. With the orbital plane precessing eastward at this rate, the ascending node will lie at a fixed local time (which is 6:00 for Wivern's orbit) [14]. The RAAN variation can be quantified by the following formula [13]:

$$\dot{\Omega} = -\frac{3}{2(1-e^2)^2} n J_2 \left(\frac{R_E}{a}\right)^2 \cos i \tag{3.2}$$

where R_E is the Earth's radius, $n = \sqrt{\mu_E/a^3}$ is the Keplerian mean motion, μ_E is the Earth gravitational parameter and a, e and i are the orbit's semi-major axis,

[1] From this point on, to simplify the notation, the vectors with no reference frame specified in the subscript are assumed in the IJK reference frame.

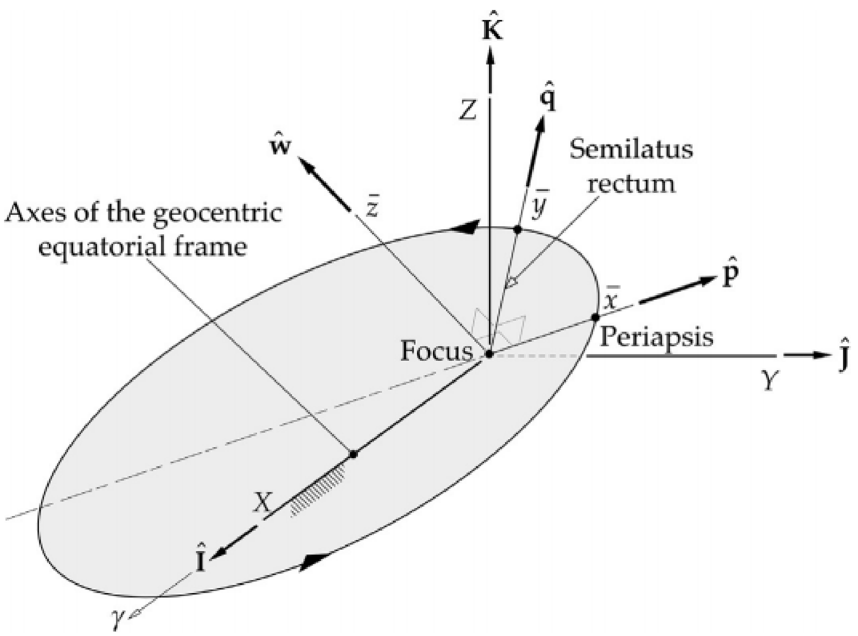

Figure 3.2: Geocentric equatorial and perifocal reference frames. [14]

eccentricity and inclination, respectively. The effects of the planet's oblateness on orbits are quantified by the dimensionless parameter J_2, the second zonal harmonic. This parameter is not a universal constant (each planet has its own value) and for the Earth $J_2 = 1.08263 \cdot 10^3$ [14]. The Earth's oblateness causes also the perturbation of the argument of perigee ω and the mean anomaly M, which will vary with the following rates [13]:

$$\dot{\omega} = \frac{3}{4(1-e^2)^2} n J_2 \left(\frac{R_E}{a}\right)^2 (5\cos^2 i - 1) \tag{3.3}$$

$$\dot{M} = n + \Delta n = n + \frac{3}{4(1-e^2)^{3/2}} n J_2 \left(\frac{R_E}{a}\right)^2 (3\cos^2 i - 1) \tag{3.4}$$

In summary, the constant orbital parameters are a, e and i, while the time-varying ones are Ω, ω and M [13]:

$$\begin{array}{lll} a(t) = a_0 & e(t) = e_0 & i(t) = i_0 \\ \Omega(t) = \Omega_0 + \dot{\Omega} t & \omega(t) = \omega_0 + \dot{\omega} t & M(t) = M_0 + \dot{M} t \end{array} \tag{3.5}$$

3.1.1 Longitude and latitude

Given at any time t the generic position vector $\vec{r} = \{x, y, z\}$ expressed in the geocentric equatorial frame, the latitude can be computed by:

$$La = \arcsin\left(\frac{z}{\|\vec{r}\|}\right) \tag{3.6}$$

And the longitude by:

$$Lo = \alpha - \alpha_G \tag{3.7}$$

where α is the right ascension of the position vector and α_G is the right ascension of the Greenwich meridian. Both these angles are measured with respect to the vernal equinox direction $\hat{\mathbf{I}}$ of the geocentric equatorial reference frame. The angle α can be retrieved by trigonometric considerations:

$$\begin{cases} \alpha = \operatorname{atan}_2(y, x) & \text{if } y \geq 0 \\ \alpha = \operatorname{atan}_2(y, x) + 2\pi & \text{if } y < 0 \end{cases} \tag{3.8}$$

Instead, the unknown term α_G in (3.7) can be obtained by:

$$\alpha_G = \alpha_{G\,ref} + \omega_{E_D}\left(t_D - t_{D\,ref}\right) + \omega_E t \tag{3.9}$$

where $\alpha_{G\,ref}$ is the Greenwich right ascension at time $t_{D\,ref}$ (expressed in Julian days), corresponding to the reference date 1 January 2000, 12:00 UT[2]. The term t_D (also in Julian days) represents instead the date at which the orbital propagation starts, while t is the time (in seconds) elapsed after the date t_D. As a consequence, ω_{E_D} is the Earth angular velocity expressed in [rad/days], while ω_E is the same angular velocity, but expressed in [rad/s].

With the present method it is possible to plot the satellite's ground track by calculating at any time t the longitude and latitude of the spacecraft position vector $\vec{r}_{sc}$. An example of ground track is shown in figure (3.3). [6][14]

3.2 Antenna pointing direction

Once the satellite positions have been computed for the whole time span, the next step is to determine the antenna boresight direction at each time instant. In the ideal case the Wivern antenna conically scans around Nadir at the off-Nadir angle $\gamma = 38°$, rotating at the angular velocity $\omega = 12$ RPM. At this stage the satellite attitude is supposed to be perfect, so the assumption that the body frame

[2]This reference date is named J2000 epoch.

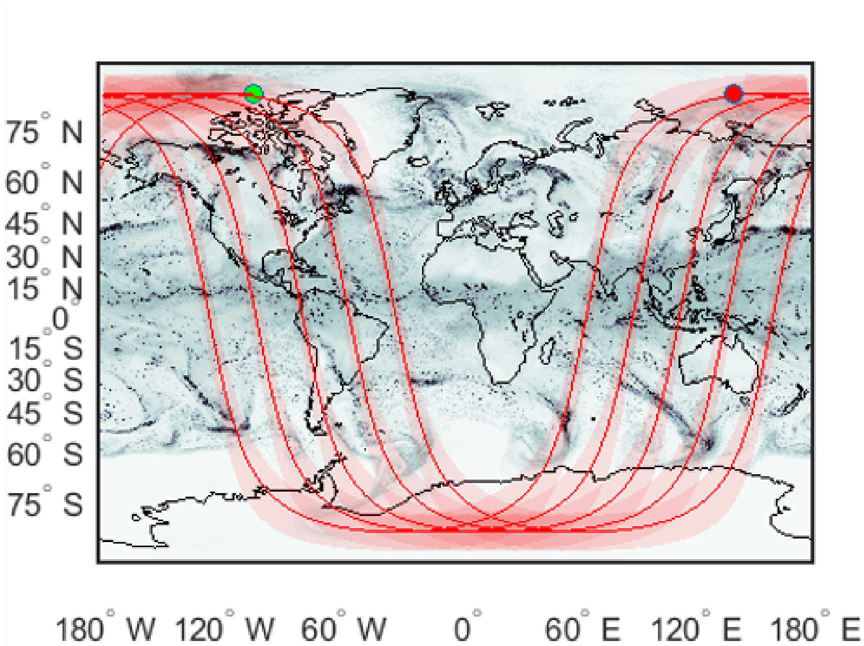

Figure 3.3: Orbit ground track.

is identical to the LVLH frame is made. The LVLH reference frame (Local-Vertical-Local-Horizontal) has its origin placed in the spacecraft's center of mass and it has the unit vectors defined as:

- $\vec{l}_1$, directed along the outward radial $\vec{r}_{sc}$;
- $\vec{l}_2$, pointing in the direction of the spacecraft's local horizon;
- $\vec{l}_3$: normal to the orbital plane.

The boresight direction can be identified at any time by the off-Nadir angle γ and by the angle δ, defined as in figure (3.5). The angle γ is constant, while δ changes in time:

$$\delta(t) = \delta_0 + \omega(t - t_0)$$

where δ_0 is the offset angle at the initial time t_0.
By the knowledge of γ and δ, the boresight unit vector can be computed at any time by the trigonometric relation:

$$\hat{u}_{bs_{LVLH}} = \begin{Bmatrix} -\cos\gamma \\ \sin\gamma\cos\delta(t) \\ \sin\gamma\sin\delta(t) \end{Bmatrix} \tag{3.10}$$

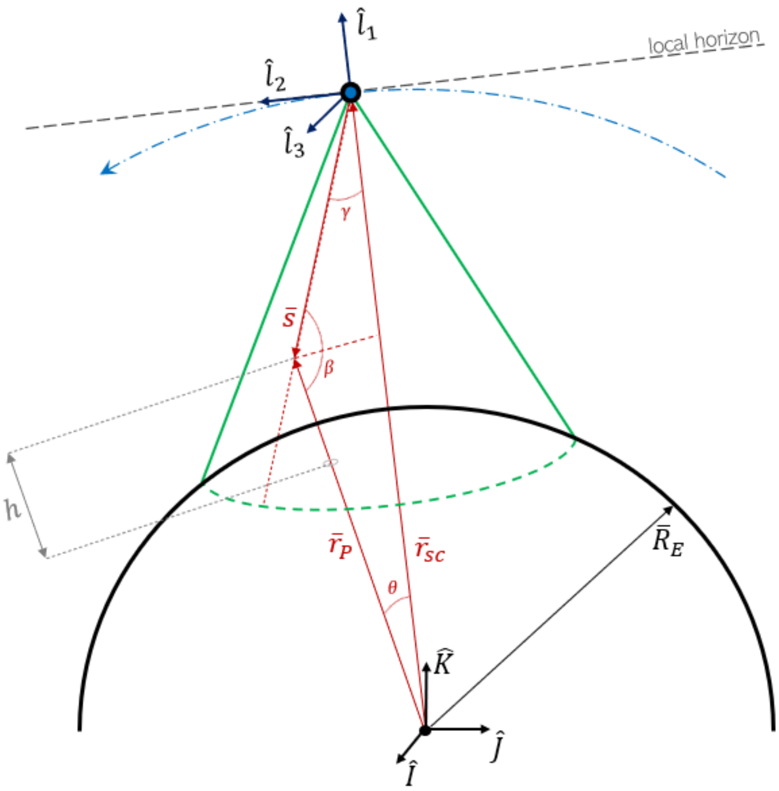

Figure 3.4: Viewing geometry.

Once the boresight direction has been identified, the only unknown term is the vector's module (or range) which can be calculated indirectly by assigning the height h at the ground. As shown in figure (3.4), the vectors $\vec{r}_{sc}$, $\vec{s}$ and $\vec{r}_P$ form a triangle that can be resolved using the *law of sines*. More specifically:

- The direction and module of $\vec{r}_{sc}$ are known;
- The direction of $\vec{s}$ is known from equation (3.10), but the range s must be calculated;
- The module of $\vec{r}_P$ is known and equals to $R_E + h$, while the direction is unknown;
- The only known angle is $\gamma = 38°$.

The angle β shown in figure (3.4) can be retrieved using the law of sines:

$$\frac{\sin\beta}{r_{sc}} = \frac{\sin\gamma}{R_E + h}$$

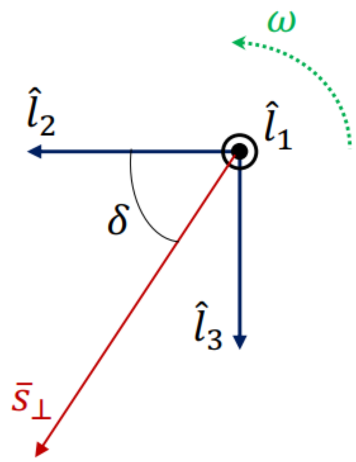

Figure 3.5: Angle δ, defined in the LVLH y-z plane. In the figure ω is the antenna angular velocity and $\overline{s}_\perp$ is the boresight vector projection on the y-z plane.

which yields:

$$\beta = \pi - \arcsin\left(r_{sc}\frac{\sin\gamma}{R_E + h}\right) \tag{3.11}$$

At this point θ can be immediately obtained by:

$$\theta = \pi - (\beta + \gamma) \tag{3.12}$$

And finally, by applying once more the law of sines, the range s can be retrieved:

$$s = \frac{R_E + h}{\sin\gamma}\sin\theta \tag{3.13}$$

Using equations (3.10) and (3.13) the boresight vector is found with respect to the LVLH frame, but it can be easily transformed in the geocentric equatorial frame by:

$$\vec{s}_{IJK} = \mathbf{L}_{LI}\vec{s}_{LVLH} \tag{3.14}$$

where $\mathbf{L}_{LI} = \mathbf{L}_3(\Omega(t))\mathbf{L}_1(i)\mathbf{L}_3(\omega(t) + \nu(t))$ is the transformation matrix, in which $\nu(t)$ the true anomaly.

3.2.1 Perturbations on azimuth

The azimuthal angle δ is subject to harmonic variations due to perturbations acting on the antenna rotation axis. The azimuth absolute knowledge error (AKE) caused by these perturbations has been estimated by industrial studies conducted for the

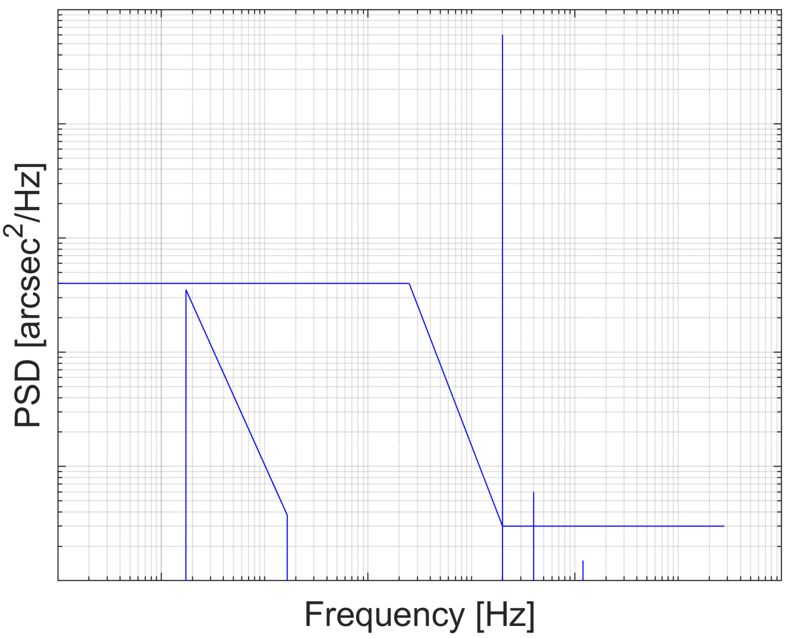

Figure 3.6: Conceptual example of the used azimuth one-sided AKE PSD. [17]

Wivern proposal [17]. This error is quantified in terms of Power Spectral Density (PSD) versus frequency, as shown in figure (3.6). From the power spectrum one can retrieve a time series using the Inverse Fast Fourier Transform algorithm (IFFT). The output signal is a discrete function which represents the azimuthal mispointing variation $\Delta\delta_{mis}$ between the real case and the ideal one, so it is possible to obtain the perturbed azimuth angle:

$$\delta_{mis}(t) = \Delta\delta_{mis}(t) + \delta(t) \tag{3.15}$$

The angle δ_{mis} can be used instead of δ in the equation (3.10) to determine the boresight direction, so the effect of mispointing can be studied with the simulator.

Numerical implementation

The one-sided PSD in figure (3.6) was recreated using a uniform frequency step Δf and a number of samples $M = N/2 + 1$, where N is the number of sampling points of the time series to be computed. Being f_c the maximum frequency[3] in the PSD, the sampling frequency must be $f_s = 2f_c$, so a sine wave at the frequency f_c

[3] f_c is the Nyquist critical frequency, defined as $f_c = 1/(2\Delta t)$ for any given Δt.

will have at least two samples per cycle. Accordingly, the sampling time step is $\Delta t = 1/f_s$, so the discrete time vector can be defined as:

$$\mathbf{t} = \Delta t \,\{0{,}1, \ldots, N-1\} \tag{3.16}$$

The discrete frequency vector can be defined knowing that the one-sided PSD is build on M discrete frequencies in the interval $[0,\ f_c]$:

$$\mathbf{f} = \underbrace{f_s/N}_{\Delta f}\{0, 1, \ldots, M-1\} \tag{3.17}$$

It must be stressed that the one-sided PSD is defined only on the positive frequencies but, in order to apply the IFFT function in Matlab, it is necessary to construct a frequency domain signal related to a two-sided PSD, which accounts also for the negative frequencies. The two-sided PSD has N values and it is constructed according to the following convention:

- the values from 1 to $M-1$ are associated with the frequencies $0 \leq f < f_c$;
- the M-th value is related to both f_c and $-f_c$;
- the values from $M+1$ to N are associated with the negative frequencies $-f_c < f < 0$.

The frequency domain signal $\mathbf{Z}$ related to this spectrum is a vector of N complex numbers, each one expressed in terms of amplitude, frequency and phase. Since the time series is supposed to be real, the vector $\mathbf{Z}$ is forced to be conjugate symmetric, so it will have the following structure:

$$\mathbf{Z} = \left\{Z_1, \ldots, Z_{M-1}, Z_M, \bar{Z}_{M-1}, \cdots, \bar{Z}_2\right\} \tag{3.18}$$

where:

$$Z_j = A_j e^{i\phi_j} \tag{3.19}$$

And $Z_j = Z(f_j)$.

By looking at equation (3.18), $\mathbf{Z}$ is completely defined by $Z_1, \ldots, Z_M$, so it is enough to calculate only these components. To compute the amplitude, the functions in figure (3.6) must be firstly added up and then multiplied by the scaling factor $f_s N$. Since the total power must be preserved, the values in the two-sided PSD shall be half the values of the one-sided PSD, except for the ones associated with the frequencies 0 and $\pm f_c$, which remain the same. By consequence, all the components $j = 2, \ldots, M-1$ must be also multiplied by a factor 0.5. Finally, the amplitude can be retrieved by applying the square root to each component, so, in summary:

$$A = \begin{cases} \sqrt{P_{\text{tot}} f_s N}, & \text{if } j = 1, M \\ \sqrt{0.5 P_{\text{tot}} f_s N}, & \text{if } j = 2, \ldots, M-1 \end{cases} \tag{3.20}$$

where P_{tot} is the sum of all the functions in figure (3.6).

The information about the phases ϕ_j of the signal cannot be obtained by the PSD plot, so a random phase in the interval $[0, 2\pi]$ is assigned to each component, except for the components related to f_1 and f_M, in which the phase is forced to be zero in order to have real numbers instead of complex ones. Finally, by applying the IFFT function to $\mathbf{Z}$, a real-valued time series can be obtained, as the one shown in figure (3.7). [23]

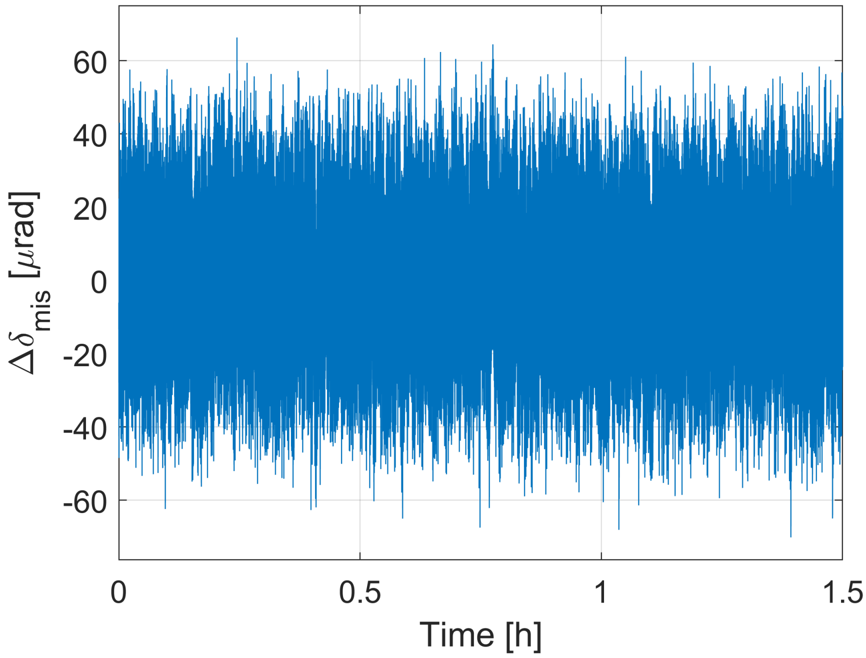

Figure 3.7: Azimuth mispointing time series.

3.3 Viewing geometry

Once the boresight pointing direction has been identified, the next step is to simulate the portion of the atmosphere and surface illuminated by the radar.

3.3.1 Atmosphere

The illuminated atmosphere volume has been defined as a cone oriented downward, with the vertex centered in the spacecraft center of mass and the axis directed along the boresight direction. The description of this volume relies on the identification of a discrete set of points identified by azimuth, polar angle with respect to the boresight direction and distance (or range) from the spacecraft:

- $N_{az} = 21$ azimuthal angles have been selected in the interval $[0,\, 2\pi]$, with a fixed step $\Delta\varphi = \frac{2\pi}{N_{az}-1}$;
- $N_{pol} = 7$ polar angles have been chosen in the interval $[0,\, \psi_{3dB}]$, with a fixed step $\Delta\psi = \frac{\psi_{3dB}}{N_{pol}-1}$;
- A set of range values has been chosen in the interval $[s_{hsup},\, s_{hinf}]$ with a fixed step $\Delta s = 0.125$ km. The initial range s_{hsup} refers to the upper height $h_{sup} = 15$ km, while s_{hinf} refers to the lower height $h_{inf} \simeq -2$ km.

The points can be generated by azimuthal/polar rotations and scaling of the boresight vector $\vec{s}$, which yield a series of vectors $\vec{d}_{V\,i\,j\,k}$ associated to the i-th range value, j-th polar angle and k-th azimuth angle. The azimuthal/polar rotations are achieved by using the concepts of *quaternion* (A.8) and rotation matrix associated to a quaternion (A.9). The rotation in azimuth is described by the quaternion:

$$\mathfrak{q}_{az} = \left\{ \cos\left(\frac{\Delta\varphi}{2}\right),\, u_{bs_1} \sin\left(\frac{\Delta\varphi}{2}\right),\, u_{bs_2} \sin\left(\frac{\Delta\varphi}{2}\right),\, u_{bs_3} \sin\left(\frac{\Delta\varphi}{2}\right) \right\}$$

where $\hat{u}_{bs} = \{u_{bs_1}, u_{bs_2}, u_{bs_3}\}$ is the unit vector of $\vec{s}$. The rotation matrix $\mathbf{T}_{az} = \mathbf{T}(\mathfrak{q}_{az})$ given by (A.9) permits the rotation of any vector around the direction of $\vec{s}$ by the angle $\Delta\varphi$. In a similar way the polar rotation can be accomplished by defining the quaternion:

$$\mathfrak{q}_{pol} = \left\{ \cos\left(\frac{\Delta\psi}{2}\right),\, u_{p_1} \sin\left(\frac{\Delta\psi}{2}\right),\, u_{p_2} \sin\left(\frac{\Delta\psi}{2}\right),\, u_{p_3} \sin\left(\frac{\Delta\psi}{2}\right) \right\}$$

where $\hat{u}_p = \{u_{p_1}, u_{p_2}, u_{p_3}\}$ is the unit vector of $\vec{p}$, which is defined as $\vec{p} = \vec{s} \times \vec{r}_{sc}$. The rotation matrix $\mathbf{T}_{pol} = \mathbf{T}(\mathfrak{q}_{pol})$ permits the rotation of a vector around the direction of $\vec{p}$ by the angle $\Delta\psi$.
Once the matrices $\mathbf{T}_{az}$ and $\mathbf{T}_{pol}$ have been calculated, the following iterative method can be applied:

1. The indices i, j, k are set to 1, so the first point of the discretization is considered.
2. The vector $\vec{d}_{V\,i\,j\,k}$ is used to start the rotations in azimuth:

   $$\vec{d}_{V\,i\,j\,k} = \mathbf{T}_{az} \vec{d}_{V\,i\,j\,k-1} \qquad \forall k = 2, \ldots, N_{az}$$

   where the azimuthal angle at each step is equal to $\varphi_k = (k-1)\Delta\varphi$. Since each vector $\vec{d}_{V\,i\,j\,k}$ is rotated by $\Delta\varphi$ with respect to the previous vector $\vec{d}_{V\,i\,j\,k-1}$, the

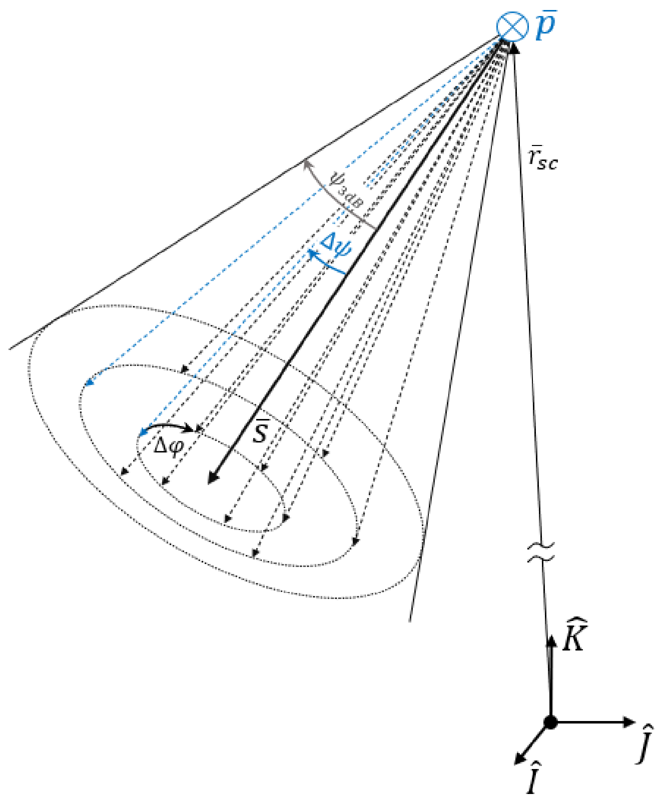

Figure 3.8: Vectors generated by azimuthal rotations (dashed black arrows) and polar rotations (light blue dashed arrows) at fixed range.

effect of these consecutive rotations is to generate a cone[4] around $\vec{s}$ with an opening angle equal to the polar angle $\psi_j = (j-1)\Delta\psi$, as shown in figure (3.8).

3. The last computed vector $\vec{d}_{V\,i\,j\,N_{az}}$ is subject to a polar rotation:

$$\vec{d}_{V\,i\,j+1\,1} = \mathbf{T}_{pol}\vec{d}_{V\,i\,j\,N_{az}}$$

4. The index j is increased by one, so the next polar angle is considered. The steps 2. and 3. are repeated while $j \leq N_{pol}$ or, in other words, when the vector $\vec{d}_{V\,i\,N_{pol}\,N_{az}}$ has been determined.

[4]The only exception is when the first polar angle $\psi_1 = 0$ rad is considered. In this case the cone degenerate on its axis, so the azimuthal rotations generate a series of identical vector directed along the boresight direction.

5. The index i is increased by 1, so the next range value is considered. In general, the vector related to the i-th range value, the first polar angle $\psi_1 = 0$ rad and the first azimuth angle $\varphi_1 = 0$ rad is given by the following relation:

$$\vec{d}_{V\,i\,1\,1} = (s_{hsup} + (i-1)\Delta s)\hat{u}_{bs}$$

6. Steps from 2. to 5. are repeated while $i \leq N_{ax}$.

3.3.2 Surface

The surface illuminated by the radar has been approximated as a plane tangent at the point of intersection between the boresight LOS and the Earth's surface. The point of intersection is also the origin of a topocentric reference frame defined as follows: starting from the South-East-Zenith ($\hat{S}\hat{E}\hat{Z}$) reference frame, an additional rotation around $\hat{Z}$ is applied in order to align $\hat{S}$ to the boresight projection on the plane. The unit vector $\hat{Z}$ remains unchanged, while $\hat{S}$ becomes $\hat{T}_1$ and $\hat{E}$ becomes $\hat{T}_2$. As a result of this additional rotation, $\hat{T}_1$, $\hat{Z}$ and the boresight LOS will lie in the same plane.

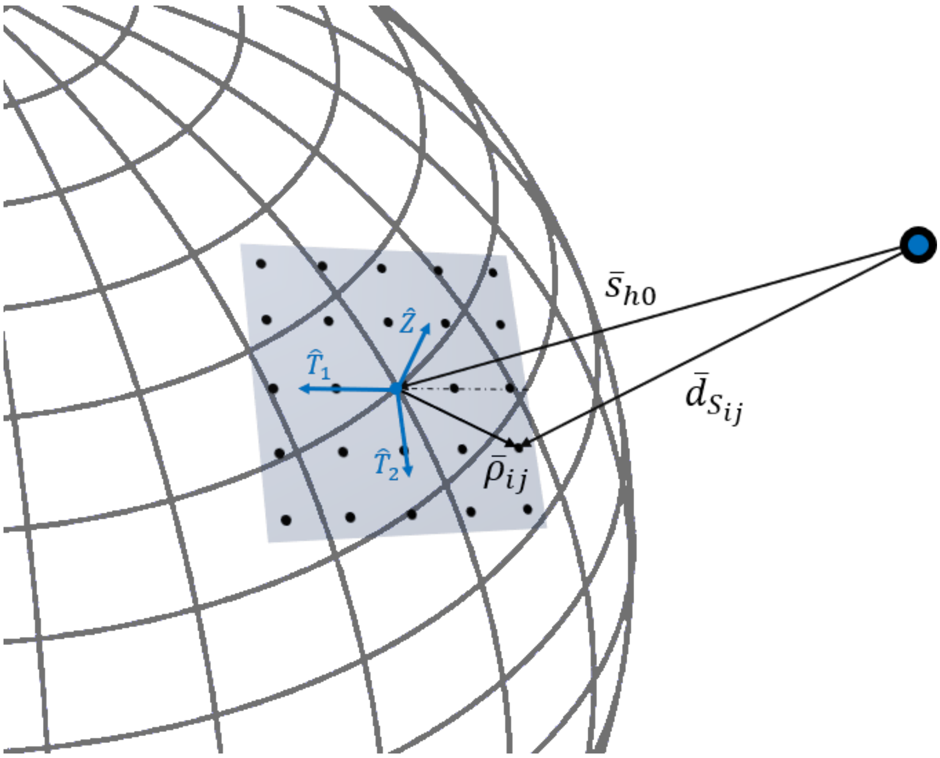

Figure 3.9: Approximation of the surface illuminated area.

A 3×3 km square grid is centered in the topocentric reference frame as shown in figure (3.9). The points are evenly spaced in both directions with a spacing of 0.1 km. Each point of the grid can be expressed in the topocentric reference frame:

$$\vec{\rho}_T = \begin{Bmatrix} x_T \\ y_T \\ 0 \end{Bmatrix} \tag{3.21}$$

And then transformed in the geocentric equatorial reference frame:

$$\vec{\rho}_{IJK} = \mathbf{L}_{TI}\vec{\rho}_T \tag{3.22}$$

The position vector of the generic point on the surface can be calculated considering the geometric relations shown in figure (3.9):

$$\vec{d}_{S\,ij} = \vec{s}_{h0} + \vec{\rho}_{ij} \tag{3.23}$$

where $\vec{s}_{h0}$ is the boresight vector related to the height $h = 0$ km.

3.3.3 Conversion from IJK to lat-lon-height

All the points discretizing the radar's viewing geometry are located in the tridimensional space by vectors $\vec{d}_{Vijk}$ and $\vec{d}_{S\,ij}$, which originate from the satellite CoM. These vectors are expressed in the geocentric equatorial reference frame but, as will be seen soon, it is essential to express them in the same coordinates of the NetCDF files data, which are latitude, longitude and height. To do so, the points must be firstly located with respect to Earth's CoM, which is done by:

$$\vec{r}_p = \vec{d} + \vec{r}_{sc} \tag{3.24}$$

where the spacecraft's CoM position $\vec{r}_{sc}$ is known from the orbit propagation. Then the latitude and longitude of $\vec{r}_p$ can be found by the equations (3.6) to (3.9), while the height is given by $h = r_p - R_E$.

3.4 Radar simulation

The purpose of the simulator is to recreate what the radar would see in a real scenario, so basic measurements of weather radars, namely measured reflectivity and Doppler velocity, shall be derived from simulation. To achieve this, it is necessary to use global models from which to extract the needed information such as equivalent reflectivity, extinction coefficient and wind velocity field, to name a few. The output data of these models are contained within NetCDF files in which a given quantity is evaluated in a set of points expressed in terms of longitude, latitude and height. As one can observe, the absence of time dependence implies that these files represent a snapshot of the atmosphere properties at a specific time. This choice has the advantage of dealing with files of smaller size, without losing any information about the weather patterns occurring at different geographical locations.

Once the global distribution of a given quantity is known, it is possible to determine its value within the radar sampling volume. However, the netCDF files are not sampled at the same points of the viewing geometry discretization, so the following procedure has been applied:

- Since the full data extrapolation from files involves a lot of memory usage, only a portion of the data is extracted at each time instant. This can be done considering that the radar viewing geometry is composed of a discrete set of points limited in terms of longitude, latitude and height, so at each time the maximum and minimum values of these coordinates can be found and used to read only the needed data.
- Reading of a NetCDF file returns a 3D array that can be used to create a function interpolating all the data within it (e.g. by using the *interpn* function in Matlab). The interpolating function is then used to determine the value of the quantity at the query points, which in this case are the points discretizing the viewing geometry.

Once this first step is complete, it is possible to simulate the radar products.

3.4.1 Reflectivity of atmospheric targets

Within the volume illuminated by the radar at time t, it may be present a certain number of atmospheric targets, each one characterized by an equivalent reflectivity Z_e^{atm}. Given the distribution of targets for the observed scene and knowing the attenuation affecting the signal, the goal is to compute the reflectivity measured by the radar. However, as mentioned in the theory chapter, at any range s the radar measures the value of reflectivity averaged over the backscattering volume $\mathcal{V}$, hence the following relation shall be used:

$$Z_{m\,\mathcal{V}}^{\mathrm{atm}}(s) = \frac{\iiint_{\mathcal{V}} Z_m^{\mathrm{atm}}\, G^2\, d\mathcal{V}}{\iiint_{\mathcal{V}} G^2\, d\mathcal{V}} \tag{3.25}$$

The squared gain G^2 accounts for the radar sensitivity on both transmission and reception and weights the reflectivity of the targets located at different polar angles. After the data interpolation, $Z_{e_{\mathrm{dB}Z}}^{\mathrm{atm}}$ and k_{ext} are known quantities at the discrete points chosen within the sampling volume, therefore equation (2.17) can be used to compute $Z_{m\mathcal{V}}^{\text{atm}}$. In practice, the integral in (2.17) can be calculated knowing that, by construction (see subsection (3.3.1)), a point at coordinates $\{s, \psi, \varphi\}$ shares the same LOS of the points located at the same azimuth φ and polar angle ψ, but different range s. Therefore, path-integration of k_{ext} along the selected LOS can be performed. The remaining term G^2 in the (3.25) is simply derived by equation (2.2), so volume integrals can be ultimately computed. Since the volume $\mathcal{V}$ has a spherical geometry, it is convenient to use range-polar-azimuth coordinates to perform integration, so the (3.25) becomes:

$$Z_{m\mathcal{V}}^{\text{atm}}(s) = \frac{\displaystyle\int_{s-\frac{\Delta r}{2}}^{s+\frac{\Delta r}{2}} \int_0^{\psi_{3\text{dB}}} \int_0^{2\pi} Z_m^{\text{atm}}(\varphi, \psi, s)\, G^2(\psi)\, s^2 \sin(\psi)\, d\varphi d\psi ds}{\displaystyle\int_{s-\frac{\Delta r}{2}}^{s+\frac{\Delta r}{2}} \int_0^{\psi_{3\text{dB}}} \int_0^{2\pi} G^2(\psi)\, s^2 \sin(\psi)\, d\varphi d\psi ds} \tag{3.26}$$

These integrals are evaluated in practice by numerical integration methods. The integrand function can be treated as a 3D array with size $N_{az} \times N_{pol} \times N_{ax}$ and then passed as input to the Matlab function *trapz*, performing trapezoidal numerical integration.

Cross-polar reflectivity of atmospheric target

The netCDF files also contain data about the equivalent cross-polar reflectivities $\mathcal{Z}_e^{\text{atm}}$ deriving from depolarization, so the method described above can also be used to calculate the measured cross-polar reflectivities $\mathcal{Z}_{m\mathcal{V}}^{\text{atm}}$(s) at any range s.

3.4.2 Reflectivity of the surface

Similarly to the atmospheric reflectivities, the value of Z_m^{surf} at range s consists of the contributions of the targets within the spherical shell with inner radius $s - \Delta r/2$ and outer radius $s + \Delta r/2$. But in this case, the targets are distributed over a surface rather than a volume, so their contribution will be determined by a surface integration. In particular, the following equation applies, being Σ the surface included within the spherical shell:

$$Z_m^{\text{surf}}(s) = \frac{\lambda^4}{\pi^6 \|K_w\|^2} \frac{8 \log 2}{\psi_{3\text{dB}}^2} \frac{s^2}{\Delta r} \iint_\Sigma \frac{\sigma_0\, f_a^2\, 10^{-\frac{2}{10}\text{PIA}}}{d^4}\, d\Sigma \tag{3.27}$$

where the term f_a^2 is equivalent to G^2 (see equation (2.2)), s is the range of the backscattering volume centre and d is the range of the surface points. Notice also that the two-ways PIA, expressed in dB, has been converted to linear units. The only new term appearing in the formula is the normalized radar cross-section (NRCS) σ_0 (in linear units), defined as the surface radar backscattering cross-section

$\sigma_{\text{surf}}^{\text{back}}$ normalized by the surface physical area A. In dB units, the NRCS is defined as:

$$\sigma_{0\,\text{dB}} \equiv 10 \log_{10} \frac{\sigma_{\text{surf}}^{\text{back}}}{A} \tag{3.28}$$

The NRCS is a measure of how efficient is the backscattering of the surface. For instance, a $\sigma_{0\,\text{dB}} > 0$ means that the surface backscatters to the radar more energy than the energy impinging onto the surface itself. The values of σ_0 depend on a certain number of parameters, first among them the type of surface being considered. For a water surface, σ_0 depends on the surface roughness and the angle of incidence. In general, with low-speed winds, σ_0 will be very high at near-Nadir incidence angles (the surface acts like a mirror) while decreasing at higher angles. This trend is still preserved for increasing surface roughness (hence higher winds speeds), but with σ_0 increasing at higher incidences and decreasing at near-Nadir angles. For land surfaces instead, the radar returns from the surface depend on the land type (e.g., urban, rural, forest) and marginally on the incidence angle. [9]

For the Wivern W-band radar configuration, characterized by a 41° off-Nadir angle at the surface, realistic ranges of value for $\sigma_{0\,\text{dB}}$ may be:

$$\begin{aligned} \sigma_{0\,\text{dB}}^{\text{sea}} &\in [-25, -22] \\ \sigma_{0\,\text{dB}}^{\text{land}} &\in [-8, -6] \end{aligned} \tag{3.29}$$

with the land generating stronger echoes than the sea.

At this point, the reflectivity of the surface at any range s can be derived by the means of equation (3.27). To solve numerically this equation, the first step is to define a discrete integration domain in which to evaluate the integrand function. This domain has already been characterized in subsection (3.3.2), and consists of a square grid with uniform spacing in both directions, as shown in figure (3.9). The integrand function contains four variables that shall be evaluated at each grid point: the normalized radar cross-section σ_0, the PIA, the beam pattern function f_a^2 and the range d. Besides the range d, which is simply equal to the module of vectors $\vec{d}_{S\,ij}$, let's analyze the other three terms:

- **NRCS**. As shown in equation (3.29), σ_0 has a strong dependence on the type of surface, so it is necessary to detect if the grid points are over land or water. The first step to accomplish this consists in locating the grid points in terms of longitude and latitude with the procedure reported in section (3.3.3). Then the coordinates of these points are linked to a global map containing the water percentage for the whole range of longitudes and latitudes. This map consists of 3600×1800 pixels of dimension $0.1° \times 0.1°$ and it associates the average water percentage of each pixel to the longitude and latitude of its centre. Since the centre of these pixels does not coincide with the surface grid points, the water percentage map is interpolated and then evaluated at the grid points, ultimately allowing the computation of σ_0 over the surface. However, there is an additional detail to consider. After interpolation, the water fraction of a grid point may be equal to 1, 0 or a value between them, which corresponds to a point being on water, land or near coastal regions, respectively. Accordingly, σ_0 is computed as the average between land and sea values, weighted by the water fraction $F_\mathrm{w} \in [0, 1]$ such that:

$$\sigma_{0\,ij} = \tilde{\sigma}_0^{\mathrm{sea}} F_{\mathrm{w}\,ij} + \tilde{\sigma}_0^{\mathrm{land}}(1 - F_{\mathrm{w}\,ij}) \tag{3.30}$$

The terms $\tilde{\sigma}_0^{\mathrm{sea}}$ and $\tilde{\sigma}_0^{\mathrm{land}}$ (in linear units) derive from picking random[5] values of $\sigma_{0\,\mathrm{dB}}$ within the ranges specified in (3.29) and converting them to linear units.

- **PIA**. In subsection (3.3.2), the only points defined are the ones of the surface, but the computation of the PIA also requires a set of points along each line of sight wherein evaluate k_{ext} and perform the path integral of equation (2.17). Consequently, along each direction identified by $\vec{d}_{S\,ij}$ (see figure (3.9)), a set of points spaced of $\Delta s = 0.125\,\mathrm{km}$ in range have been chosen within the range interval $[d_{S\,ij} - 20,\, d_{S\,ij}]$ (in km). This additional operation allows the computing of the PIA for all the grid points.

- **Antenna pattern function**. The function $f_a^2(\psi)$ defined in (2.2) depends only on the polar angle ψ of the line of sight, which is calculated as the scalar product between the LOS and boresight unit vector:

$$\psi_{ij} = \arccos\left(\hat{u}_{d_{S\,ij}} \bullet \hat{u}_{bs}\right) \tag{3.31}$$

  being $\hat{u}_{d_{S\,ij}} = \vec{d}_{S\,ij} / \|\vec{d}_{S\,ij}\|$.

At this stage, it is finally possible to evaluate the integrand function over the grid and numerically resolve the double integral of the equation (3.27). In principle, the domain Σ at range s should be the surface region within the spherical shell with radius between $s - \Delta r/2$ and $s + \Delta r/2$, but practically it is easier to set to zero all the terms of the integrand function related to points outside the spherical shell and directly evaluating the integral over the total grid area.

Cross-polar reflectivity of the surface

The above procedure can be used to quantify the cross-polar return of the surface by considering different values of the NRCS. The depolarization caused by water

[5] More precisely, two values $\tilde{\sigma}_{0\,\mathrm{dB}}^{\mathrm{sea}}$ and $\tilde{\sigma}_{0\,\mathrm{dB}}^{\mathrm{land}}$ are taken at each time step when creating a new surface grid, but they don't vary among the points of the same grid.

and land surfaces can be quantified by the following LDRs:

$$\begin{array}{lcl} \mathrm{LDR}_{\mathrm{dB}}^{\mathrm{sea}} & \in & [-14, -13] \\ \mathrm{LDR}_{\mathrm{dB}}^{\mathrm{land}} & \in & [-6, -5] \end{array} \tag{3.32}$$

Equation (3.30) is then modified as follows:

$$\varsigma_{0\,ij} = \left(\tilde{\sigma}_0^{\mathrm{sea}} + \widetilde{\mathrm{LDR}}^{\mathrm{sea}}\right) F_{\mathrm{w}\,ij} + \left(\tilde{\sigma}_0^{\mathrm{land}} + \widetilde{\mathrm{LDR}}^{\mathrm{land}}\right)(1 - F_{\mathrm{w}\,ij}) \tag{3.33}$$

where the values of $\tilde{\sigma}_0$ and $\widetilde{\mathrm{LDR}}$ derive from choosing random numbers in the intervals (3.29) and (3.32) and then converting them to linear units. Replacing σ_0 in equation (3.27) with the linear cross-polar NRCS ς_0 yields ultimately the cross-polar reflectivity of the surface $\mathcal{Z}_m^{\mathrm{surf}}(\mathrm{s})$.

3.4.3 Doppler velocity of atmospheric targets

The primary objective of the simulator is to derive the line of sight velocities of the targets within the radar observation volume. For atmospheric targets, the Doppler velocity at a range s is calculated as a weighted average within the backscattering volume $\mathcal{V}$, in the same fashion as reflectivities in (3.25):

$$v_{D_{\mathcal{V}}}^{\mathrm{atm}}(s) = \frac{\iiint_{\mathcal{V}} v_r^{\mathrm{atm}}\, Z_m^{\mathrm{atm}}\, G^2\, d\mathcal{V}}{\iiint_{\mathcal{V}} Z_m^{\mathrm{atm}}\, G^2\, d\mathcal{V}} - \vec{v}_{sc} \bullet \hat{u}_{bs} \tag{3.34}$$

being $\vec{v}_{sc} \bullet \hat{u}_{bs}$ the projection of the satellite velocity along the boresight direction[6]. The variable v_r^{atm} appearing in the relation represents the measured target radial velocity along the line of sight and it is weighted by the squared antenna gain and the reflectivity. As usual, the term G^2 accounts for the variable sensitivity of the antenna in transmission and reception for different polar angles, while the reflectivity Z_m^{atm} weights differently the radial velocities of targets depending on the strength of their echoes. The term Z_m^{atm} also removes the contributions from clear sky regions ($Z_m^{\mathrm{atm}} = 0$), where the W-band radar cannot see. If the radar could measure the same winds from a non-moving platform ($\vec{v}_{sc} = 0$) regardless of the value of reflectivity, the ideal LOS velocity would be:

$$v_{AW_{\mathcal{V}}}^{\mathrm{atm}}(s) = \frac{\iiint_{\mathcal{V}} v_{r0}^{\mathrm{atm}}\, G^2\, d\mathcal{V}}{\iiint_{\mathcal{V}} G^2\, d\mathcal{V}} \tag{3.35}$$

[6]Note that both $\vec{v}_{sc}$ and $\hat{u}_{bs}$ depend only on time, so their scalar product is constant within each sampling volume.

To resolve both equations (3.34) and (3.35), the radial velocity components v_r^{atm} and v_{r0}^{atm} within $\mathcal{V}$ are needed. The netCDF files contain information about the global wind field, so the data can be extracted and used to evaluate the three components of the wind in each point of the sampling volume. The winds components U, V, W are defined in a meteorological reference frame with the following convention:

- The first component U is the West-East wind, with positive values while pointing East;
- The second component V is South-North wind, with positive values while pointing North;
- The third component W is the wind along the local vertical, with positive values while pointing Zenith.

The above-defined reference frame is basically a $\hat{S}\hat{E}\hat{Z}$ rotated by a counterclockwise 90° rotation about the $\hat{Z}$ axis. Without defining additional reference frames, it is equivalent to use the $\hat{S}\hat{E}\hat{Z}$ coordinate system, but defining the wind velocity vector as $\vec{v}_{w_{SEZ}} = \{-V, U, W\}$ to account for the different convention. The vector $\vec{v}_{w_{SEZ}}$ is then a known quantity at each point of the sampling volume, but a coordinates transformation is still needed to perform operations with other vectors expressed, by choice, in IJK coordinates, hence:

$$\vec{v}_{w_{IJK}} = \mathbf{L}_{SI}\vec{v}_{w_{SEZ}} \tag{3.36}$$

where $\mathbf{L}_{SI}$ is the transformation matrix from SEZ to IJK.

Since the transmitted signal originates from a moving platform, the measured Doppler velocity will also detect a component of the satellite velocity along the line of sight, other than the LOS speed of the targets. As a result, the measured radial velocity of a target will be the sum of these two contributions:

$$v_r^{\mathrm{atm}} = \underbrace{(\vec{v}_{sc} \bullet \hat{u}_{d_V})}_{satellite} + \underbrace{(\vec{v}_w \bullet \hat{u}_{d_V})}_{wind} \tag{3.37}$$

being $\hat{u}_{d_V}$ the LOS unit vector. This implies that the actual radial velocity of targets can be obtained only after removing the radial component of the satellite velocity, thus justifying the term $\vec{v}_{sc} \bullet \hat{u}_{bs}$ appearing in equation (3.34). On the other hand, since equation (3.35) assumes a satellite velocity equal to zero, the radial velocity will be:

$$v_{r0}^{\mathrm{atm}} = \underbrace{(\cancel{\vec{v}_{sc} \bullet \hat{u}_{d_V}})}_{satellite} + \underbrace{(\vec{v}_w \bullet \hat{u}_{d_V})}_{wind} \tag{3.38}$$

In practice, equations (3.37) and (3.38) must be applied for all the sampling points defined in subsection (3.3.1), thus obtaining two different 3D arrays of size

$N_{az} \times N_{pol} \times N_{ax}$ containing all the radial velocities. Since both the wind velocity vector $\vec{v}_{w_{ijk}}$ and the LOS direction $\hat{u}_{d_{Vijk}} = \vec{d}_{Vijk}/\|\vec{d}_{Vijk}\|$ are known at these points, the radial velocities $v^{\text{atm}}_{r_{ijk}}$ and $v^{\text{atm}}_{r0_{ijk}}$ can be easily derived. In the end, the volume integrals of equations (3.34) and (3.35) can be converted to polar coordinates as done for the reflectivities, thus rewriting $v^{\text{atm}}_{D_{\mathcal{V}}}(s)$ as:

$$v^{\text{atm}}_{D_{\mathcal{V}}}(s) = \frac{\displaystyle\int_{s-\frac{\Delta r}{2}}^{s+\frac{\Delta r}{2}} \int_0^{\psi_{3\text{dB}}} \int_0^{2\pi} v_r^{\text{atm}}(\varphi,\psi,s)\, Z_m^{\text{atm}}(\varphi,\psi,s)\, G^2(\psi)\, s^2 \sin(\psi)\, d\varphi d\psi ds}{\displaystyle\int_{s-\frac{\Delta r}{2}}^{s+\frac{\Delta r}{2}} \int_0^{\psi_{3\text{dB}}} \int_0^{2\pi} Z_m^{\text{atm}}(\varphi,\psi,s)\, G^2(\psi)\, s^2 \sin(\psi)\, d\varphi d\psi ds} \dots$$

$$\dots - \vec{v}_{sc} \bullet \hat{u}_{bs} \tag{3.39}$$

and $v^{\text{atm}}_{AW_{\mathcal{V}}}(s)$ as:

$$v^{\text{atm}}_{AW_{\mathcal{V}}}(s) = \frac{\displaystyle\int_{s-\frac{\Delta r}{2}}^{s+\frac{\Delta r}{2}} \int_0^{\psi_{3\text{dB}}} \int_0^{2\pi} v_{r0}^{\text{atm}}(\varphi,\psi,s)\, G^2(\psi)\, s^2 \sin(\psi)\, d\varphi d\psi ds}{\displaystyle\int_{s-\frac{\Delta r}{2}}^{s+\frac{\Delta r}{2}} \int_0^{\psi_{3\text{dB}}} \int_0^{2\pi} G^2(\psi)\, s^2 \sin(\psi)\, d\varphi d\psi ds} \tag{3.40}$$

3.4.4 Doppler velocity of the surface

The Doppler associated to the surface is given by:

$$v_D^{\text{surf}}(s) = \frac{\dfrac{\lambda^4}{\pi^6\|K_w\|^2} \dfrac{8\log 2}{\psi^2_{3\text{dB}}} \dfrac{s^2}{\Delta r} \displaystyle\iint_\Sigma \frac{v_r^{\text{surf}}\, \sigma_0\, f_a^2\, 10^{-\frac{2}{10}\text{PIA}}}{d^4}\, d\Sigma}{Z_m^{\text{surf}}(s)} - \vec{v}_{sc} \bullet \hat{u}_{bs} \tag{3.41}$$

The equation structure is equivalent to the one used to compute $Z_m^{\text{surf}}(s)$ and hence resolved with the same procedure illustrated in subsection (3.4.2). The only unknown term is the measured radial velocity of the surface v_r^{surf}, which is given for each grid point (figure (3.9)) by:

$$v_r^{\text{surf}} = \underbrace{(\vec{v}_{sc} \bullet \hat{u}_{d_S})}_{satellite} + \underbrace{(\cancel{\vec{v}_S \bullet \hat{u}_{d_S}})}_{surface} \tag{3.42}$$

As a first approximation, the actual velocity of the surface $\vec{v}_S$ is assumed to be zero everywhere, which means that the only remaining term is the component of the satellite velocity along each the line of sight $\hat{u}_{d_{S\,ij}}$.

3.4.5 Total Doppler velocity

The total Doppler velocity is calculated as the reflectivity weighted average of the surface and atmospheric Doppler velocities:

$$v_D^{\mathrm{tot}}(s) = \frac{v_{D\mathcal{V}}^{\mathrm{atm}}(s)\, Z_{m\mathcal{V}}^{\mathrm{atm}}(s) + v_D^{\mathrm{surf}}(s)\, Z_m^{\mathrm{surf}}(s)}{Z_m^{\mathrm{tot}}(s)} \tag{3.43}$$

where all the reflectivities are in linear units and $Z_m^{\mathrm{tot}}(s) = Z_{m\mathcal{V}}^{\mathrm{atm}}(s) + Z_m^{\mathrm{surf}}(s)$.

3.4.6 LDR

Once the copolar and cross-polar reflectivities are known, the LDR computation is immediate and follows directly from its definition (2.18):

$$\mathrm{LDR}_{\mathrm{dB}}(s) = \mathcal{Z}_{m\,\mathrm{dB}Z}^{\mathrm{tot}}(s) - Z_{m\,\mathrm{dB}Z}^{\mathrm{tot}}(s) \tag{3.44}$$

being $\mathcal{Z}_m^{\mathrm{tot}}(s) = \mathcal{Z}_{m\mathcal{V}}^{\mathrm{atm}}(s) + \mathcal{Z}_m^{\mathrm{surf}}(s)$ the total cross-polar reflectivity in linear units at range s. Note that in equation (3.44) the reflectivities must be converted in dB units prior to subtraction.

3.4.7 Ghosts

The implementation of ghosts follows directly from the considerations made in subsection (2.4.2). Assuming $Z_{\mathrm{HH}} = Z_{\mathrm{VV}} = Z_m^{\mathrm{tot}}$ and $\mathcal{Z}_{\mathrm{HV}} = \mathcal{Z}_{\mathrm{VH}} = \mathcal{Z}_m^{\mathrm{tot}}$, then the reflectivity measured in the first channel (H or V indifferently) comprehensive of both copolar and cross-polar signals is:

$$\mathrm{Z}_1(s) = Z_m^{\mathrm{tot}}(s) + \mathcal{Z}_m^{\mathrm{tot}}(s - cT_{\mathrm{hv}}/2) \tag{3.45}$$

while the reflectivity measured in the second channel at the orthogonal polarization is given by:

$$\mathrm{Z}_2(s) = Z_m^{\mathrm{tot}}(s) + \mathcal{Z}_m^{\mathrm{tot}}(s + cT_{\mathrm{hv}}/2) \tag{3.46}$$

The average reflectivity measured from the two channels will be:

$$\mathrm{Z}_{12}(s) = 0.5\,[\mathrm{Z}_1(s) + \mathrm{Z}_2(s)] \tag{3.47}$$

3.4.8 Noise on Doppler velocity

The noise added to the total Doppler velocities v_D^{tot} is computed with the procedure shown in subsection (2.4.3), where Z_{co} refer to Z_m^{tot} and Z_{cx} to $\mathcal{Z}_m^{\mathrm{tot}}$ (using the current notation). For the present simulation a time step of 2 ms has been considered, time in which M= 8 pulse pairs are fired and a corresponding distance of 1 km is covered by the footprint. The results obtained at each time will then correspond to an averaging over M= 8 samples that will reduce the variance (2.22) and hence the noise. In the end, a Gaussian random noise with standard deviation equal to (2.22) is added to the velocities, which are then folded back into the Nyquist interval, $v_{r\,\max} = \frac{\lambda}{4T_{\text{hv}}}$. [12][16][22]

3.4.9 Mispointing

The procedure described in subsection (3.2.1) returns a time series of the error $\Delta\delta_{mis}$ affecting the azimuth (figure (3.7)). From the knowledge of $\Delta\delta_{mis}$ over time, the mispointing azimuth angle δ_{mis} can be easily derived from equation (3.15). Substituting δ_{mis} in equation (3.10) yields the mispointed boresight unit vector in LVLH coordinates, successively transformed in IJK coordinates through the transformation matrix $\mathbf{L}_{LI}$. Since the Doppler velocities are derived after subtracting the satellite velocity component along the boresight direction, the imperfect knowledge of the latter will lead to an erroneous estimate of the radial component of the satellite speed. Consequentially, this will generate an error on the Doppler velocity, quantified by the following relation:

$$\Delta \text{v}_{mis} = \vec{v}_{sc} \bullet \hat{u}_{bs\,mis} - \vec{v}_{sc} \bullet \hat{u}_{bs} \tag{3.48}$$

where all the vectors are expressed in IJK coordinates.

3.4.10 NUBF and wind shear

An estimate of the error caused by the non-uniform beam filling is given by:

$$\Delta v_{\text{NUBF}} = v^{\text{atm}}_{D\,\mathcal{V}} - v^{\text{atm}}_{D0\,\mathcal{V}} \tag{3.49}$$

where $v^{\text{atm}}_{D0\,\mathcal{V}}$ is a theoretical Doppler velocity computed in the same way as $v^{\text{atm}}_{D\,\mathcal{V}}$, but setting to zero the speed of the moving platform ($\vec{v}_{sc} = 0$). [7]

Similarly to NUBF, biases in winds measurements may arise when there is a large vertical gradient of radar reflectivity across the radar backscattering volume coupled with vertical wind shear. The errors can be estimated by:

$$\Delta v_{\text{wind shear}} = v^{\text{atm}}_{D0\,\mathcal{V}} - v^{\text{atm}}_{AW\,\mathcal{V}} \tag{3.50}$$

where in both terms the satellite velocity is assumed to be zero. [7]

Chapter 4

Results

This chapter showcases the outputs of the E2E simulator, fully implemented in the Matlab development environment. At first, multiple orbits propagation has been carried out to determine the observing cycle. Then, the orbital model has been linked to a stationary atmosphere model to perform radar simulations. For a simpler and more intuitive interpretation of the results, the simulation has been performed on a short time scale over a selected region of interest.

Apart from the first graphs regarding the orbit and the scene selection, most of the figures derived from simulation (i.e., figure (4.5)) present the following structure:

- The x-axis represents the temporal scale of the plots, implicitly displaying the time evolution as distance travelled along the scanning track or azimuth angle δ formed by the boresight direction with the local horizontal of the LVLH reference frame (coincident with the satellite velocity for a circular orbit). Both azimuth and covered footprint distance values refer to a time discretization with step $\Delta t = 2\,\text{ms}$ (equal to a total of M $= 8$ pulse pairs fired with a PRI $= 250\,\mu\text{s}$) and time interval $[0, 5]\,\text{s}$. Within the time of $5\,\text{s}$, corresponding to a single full scan, the footprint travels a distance of $\simeq 2500\,\text{km}$, while the azimuth δ covers an angle of $360°$.

- The y-axis represents the spatial variation along the slant path with the range discretization defined in subsection (3.3.1). Each range s is then converted to the corresponding height h to obtain an altitude scale. For the selected range discretization, heights span from a maximum of $15\,\text{km}$ to a minimum of $\simeq -2\,\text{km}$.

- The colour bar displays the values of the quantity of interest.

4.1 Revisit time

The simulator implements an orbital model with the initial orbital parameters equal to the mean elements listed in table (1.2) and perturbations due to the J2 effect. The resulting orbit is Sun-synchronous and completes 15 + 1/5 orbits a day with a ground track repeat cycle of 5 days. The satellite altitude ranges between 500-515 km, with a corresponding swath of roughly 800 km. As shown in figures (4.1) and (4.2), the maximum possible delay between two consecutive observations occurs at near-equatorial latitudes, wherein Wivern could take up to almost 4 days to revisit the same location. Figure (4.2) also illustrates the mean revisit times, showing an average of roughly 1.4 days at near-equatorial latitudes and less than 1 day for latitudes above 50° and below −50°. These results are consistent with the expected observing cycle performances indicated in chapter one and derived from industrial studies.

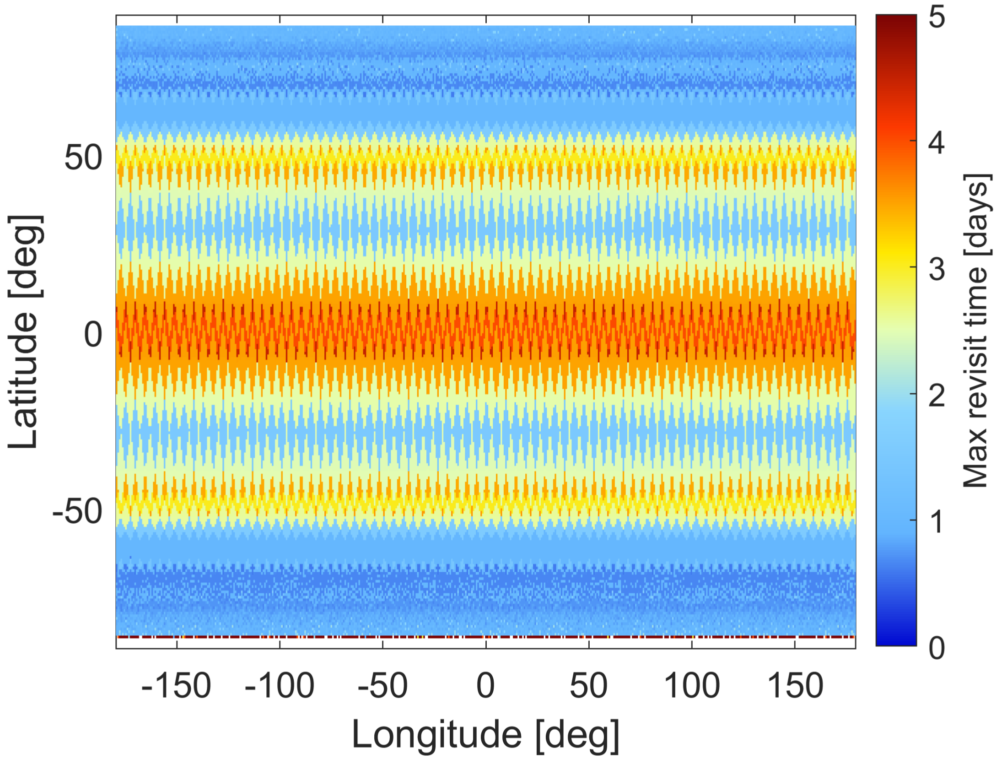

Figure 4.1: Colourmap of max revisit times for a 20 days orbit propagation.

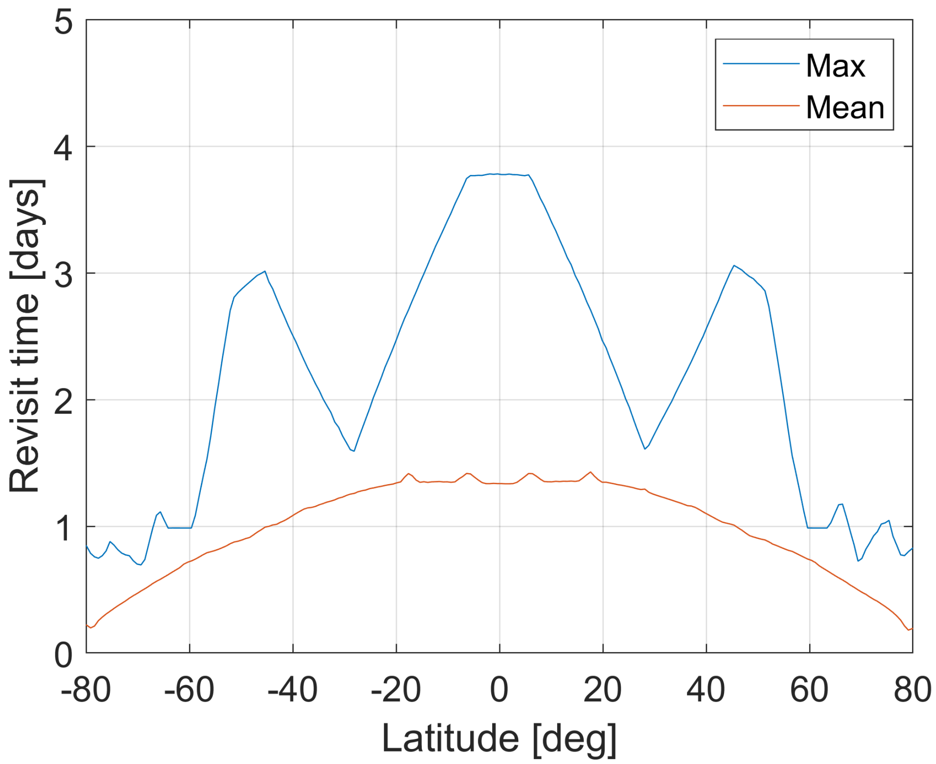

Figure 4.2: Max and mean revisit times for a 20 days orbit propagation.

4.2 Case study: scene over Labrador

The simulator features are demonstrated for a satellite flyover above Labrador, Canada. As depicted in figure (4.3), the satellite is moving in the north-northwest direction performing multiple scans over the region.

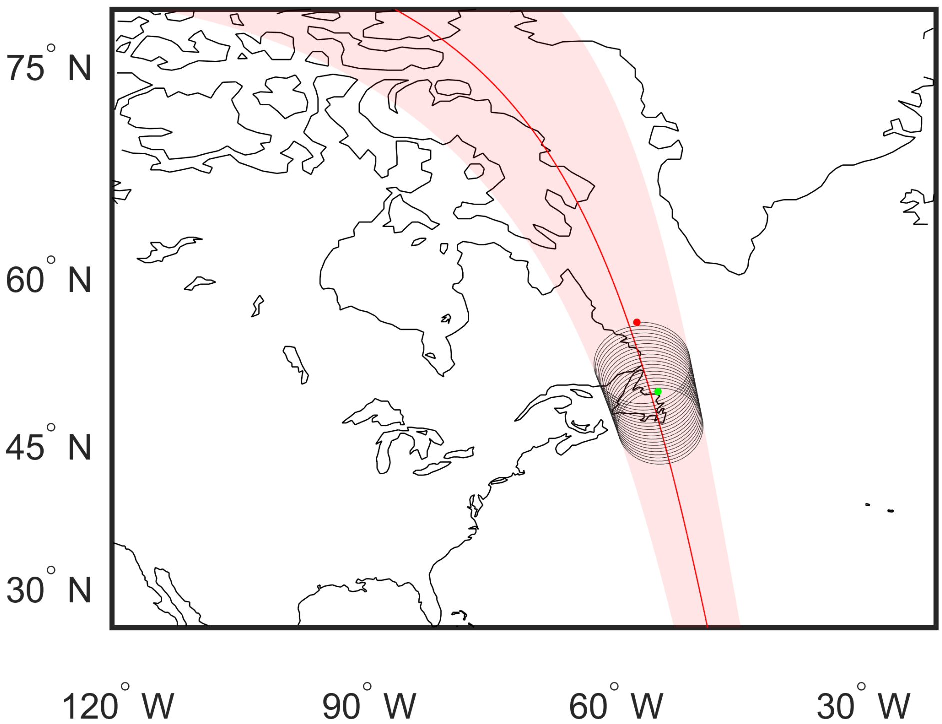

Figure 4.3: Wivern overpass above Labrador. The red line represents the satellite ground track, while the grey line represents a portion of the footprint with the radar scanning counterclockwise from the green to the red dot. The red-shaded area represents the scanning swath.

Considering that a simulation over multiple scans would lead to a less clear visualization of the results, a single scan simulation of duration $T_{\text{scan}} = 5\,\text{s}$ has been chosen instead. Figure (4.4) illustrates the situation: as it moves northward with the satellite, the radar completes a full scan over the region with its footprint intercepting both land and sea surfaces. The selection of a coastal area is not a coincidence since it allows visualizing the returns from different types of surfaces. But more importantly, the region shows a significant presence of atmospheric targets, as suggested by the high values of the path-integrated attenuation (dark areas in the figure) at the end of the scanning track. It is possible to reach the same conclusions from figure (4.5), which displays the antenna weighted hydrometeors content along the line of sight. The figure shows indeed the presence of a variety of clouds and liquid and solid precipitation mainly concentrated at the end (and partially at the beginning) of the cycloidal scanning path for the lower altitudes.

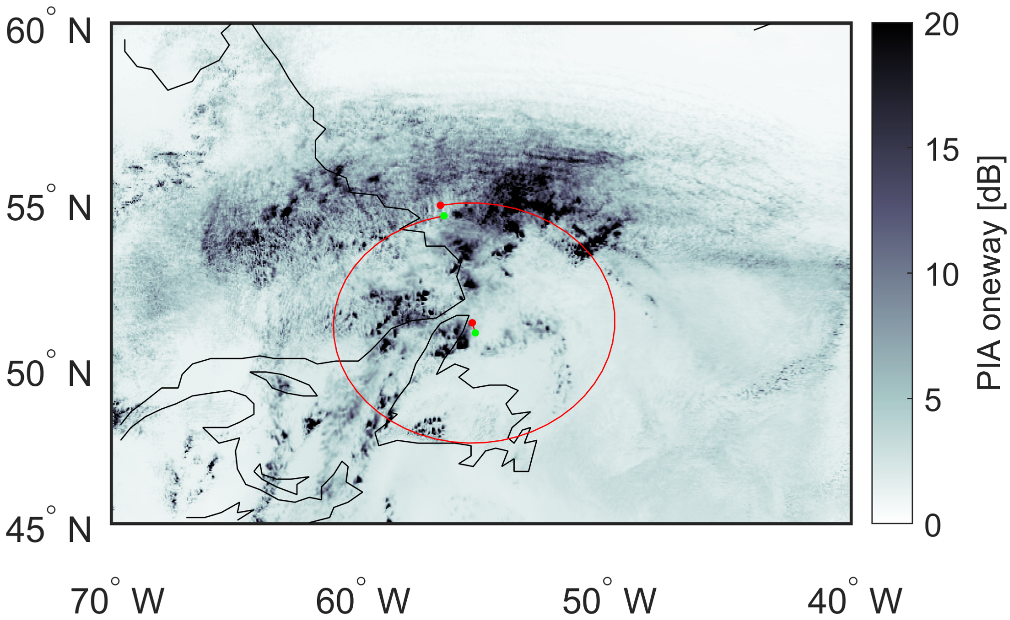

Figure 4.4: Single scan footprint (red cycloidal path) and satellite ground track (short red line at the centre) above the selected region. The colourmap displays the PIA values computed as the oneway integration along the topocentric local verticals.

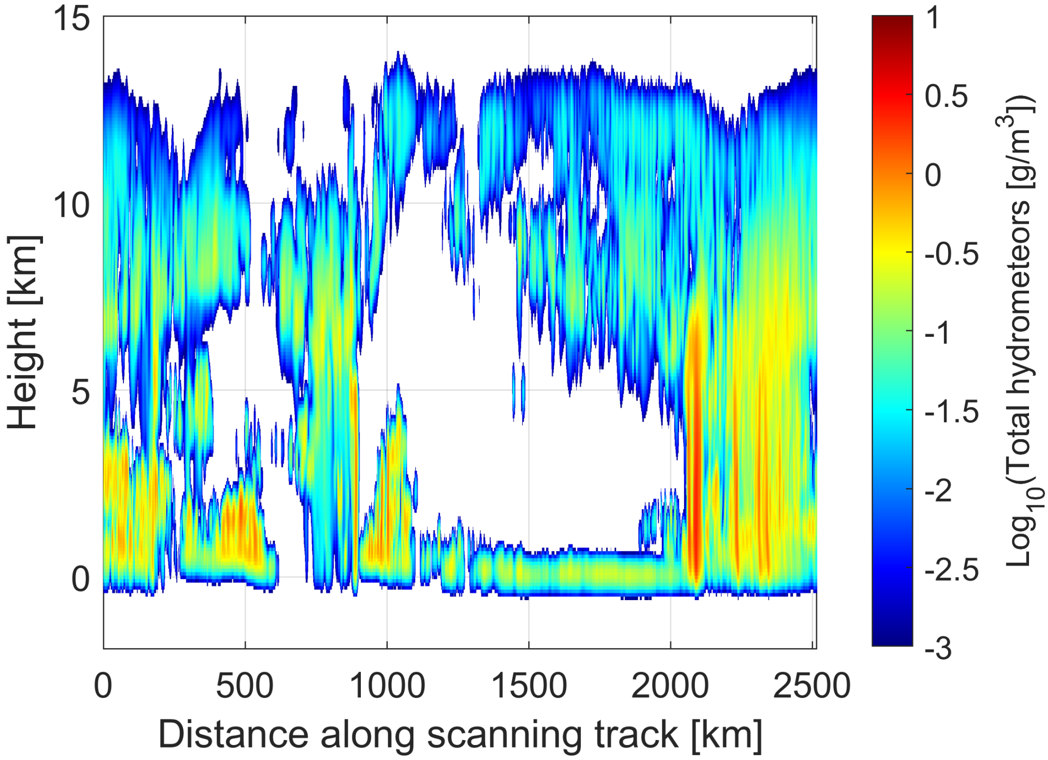

Figure 4.5: Antenna weighted hydrometeors content in g/m^3 expressed in base-10 logarithmic scale.

Figure (4.6) shows the mean atmospheric reflectivities $Z_{m\nu}^{\text{atm}}$ with values higher than $-30\,\text{dB}Z$. The slant path profiles derives from the procedure reported in subsection (3.4.1), where for each time instant (corresponding to a certain distance covered by the footprint) the formula (3.26) is applied for the selected set of ranges. As one can observe, figure (4.6) mirrors figure (4.5), with large reflectivity values generally found in areas with high hydrometeors content. Of particular interest is the region from 2000 to 2500 km along the scanning track, which shows a strong attenuation of the signal coming from heights between 0 and 2 km. The signals reaching the lower altitudes must indeed travel back and forth through a broad region with intense precipitation, so low reflectivity values are measured despite the high hydrometeors content.

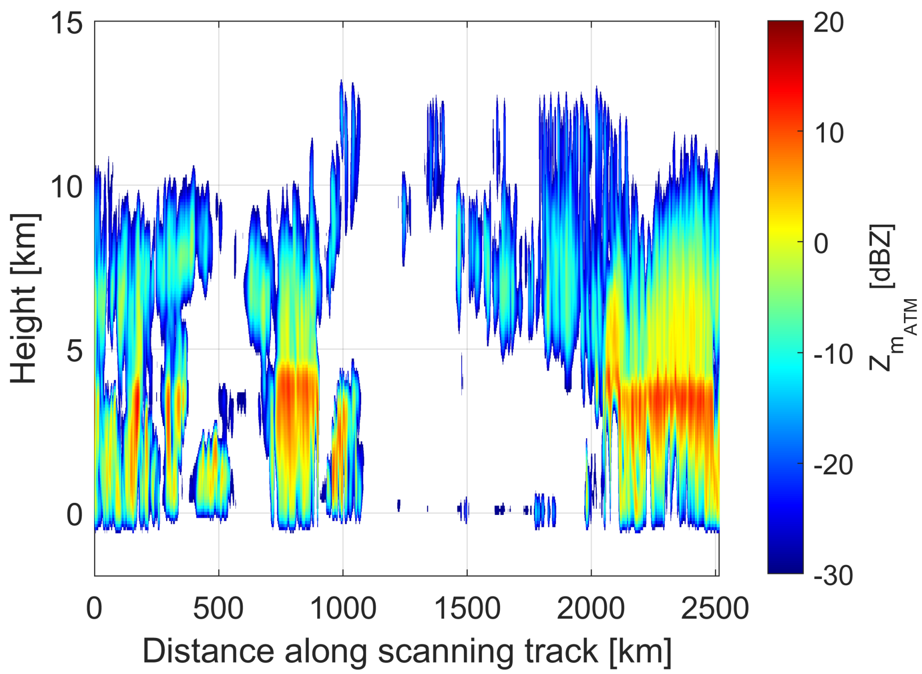

Figure 4.6: Atmospheric reflectivities.

The atmospheric reflectivities illustrated in the last image identify the regions returning the echoes detectable by the radar. From these returns, the radar measures the Doppler velocities of the targets. If the radar could ideally see everywhere, the mean LOS velocities, denoted by $v_{AW\nu}^{\text{atm}}$, would be the ones depicted in figure (4.7). The image displays a considerable LOS velocity variability along the scanning track, which shall be actually attributed to the antenna rotation (and consequent change of the LOS direction), rather than to significant winds variations.

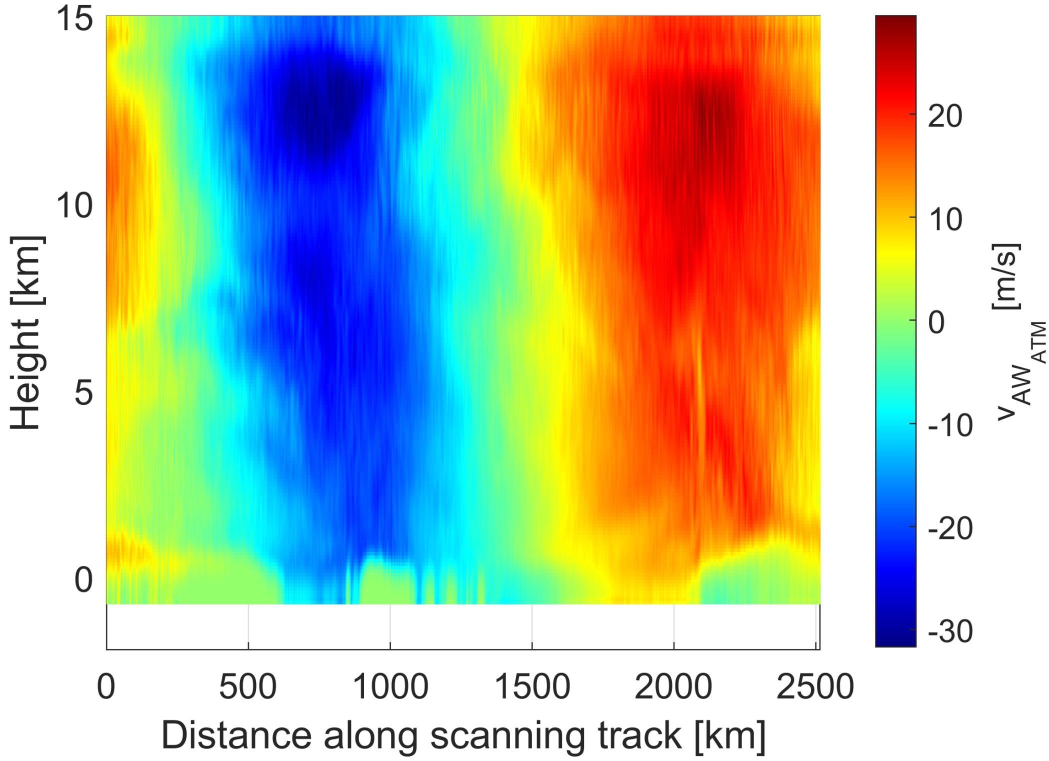

Figure 4.7: Ideal LOS winds.

The actual Doppler velocities, denoted by $v_{D_\mathcal{V}}^{\mathrm{atm}}$ and computed by means of equation (3.39), are plotted in figure (4.8). The image shows only the results where the reflectivities are above $-30\,\mathrm{dB}Z$ and hence it matches with figure (4.6).

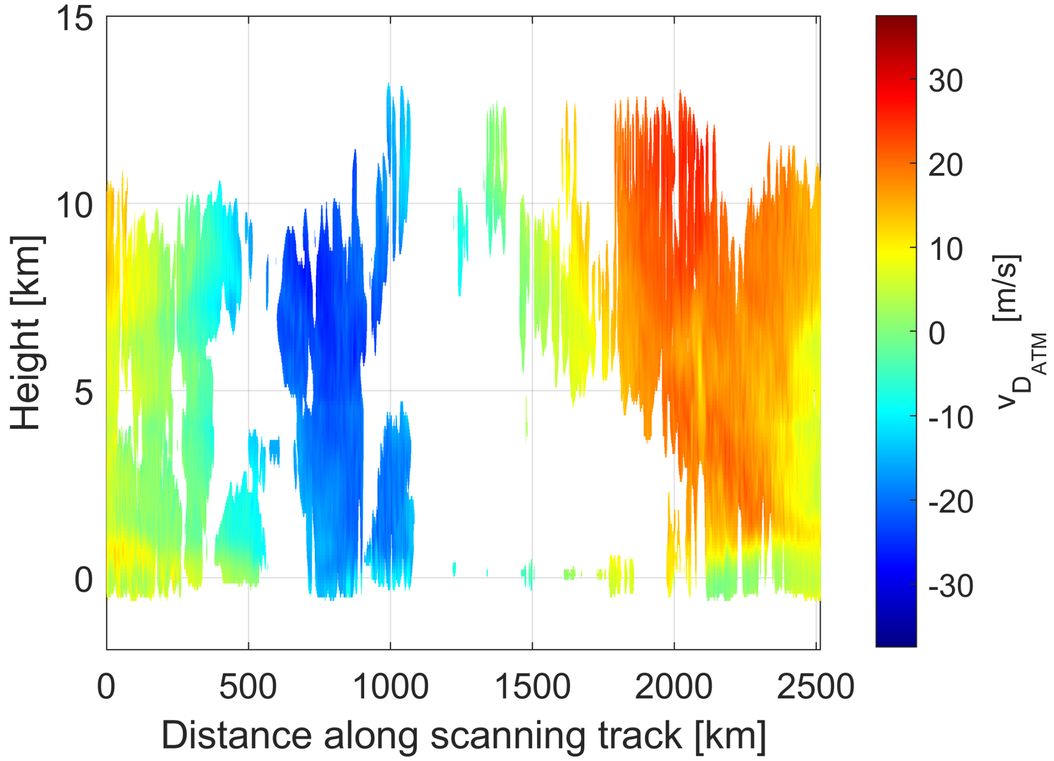

Figure 4.8: Doppler velocities of atmospheric targets.

Figure (4.9) displays the reflectivity of the surface with values higher than $-30\,\mathrm{dB}Z$. The y-axis is scaled to the interval where the surface contribution becomes significant, which spans from -1 to $1\,\mathrm{km}$ for the selected Wivern looking geometry and antenna pattern. Note that reflectivities located at negative altitudes refer to backscattering volumes with centre below the surface, but still intercepting the latter because of the slant geometry. The image shows a marked variability due to the different σ_0 values related to land and sea surfaces, as defined in (3.29). The comparison between figures (4.4) and (4.9) shows, as expected, that high reflectivities correspond to the footprint passage over land, while lower values identify the returns from water surfaces. From 2000 to 2500 km the surface returns very faint echoes (even below the threshold value of $-30\,\mathrm{dB}Z$) due to strong path-integrated attenuation.

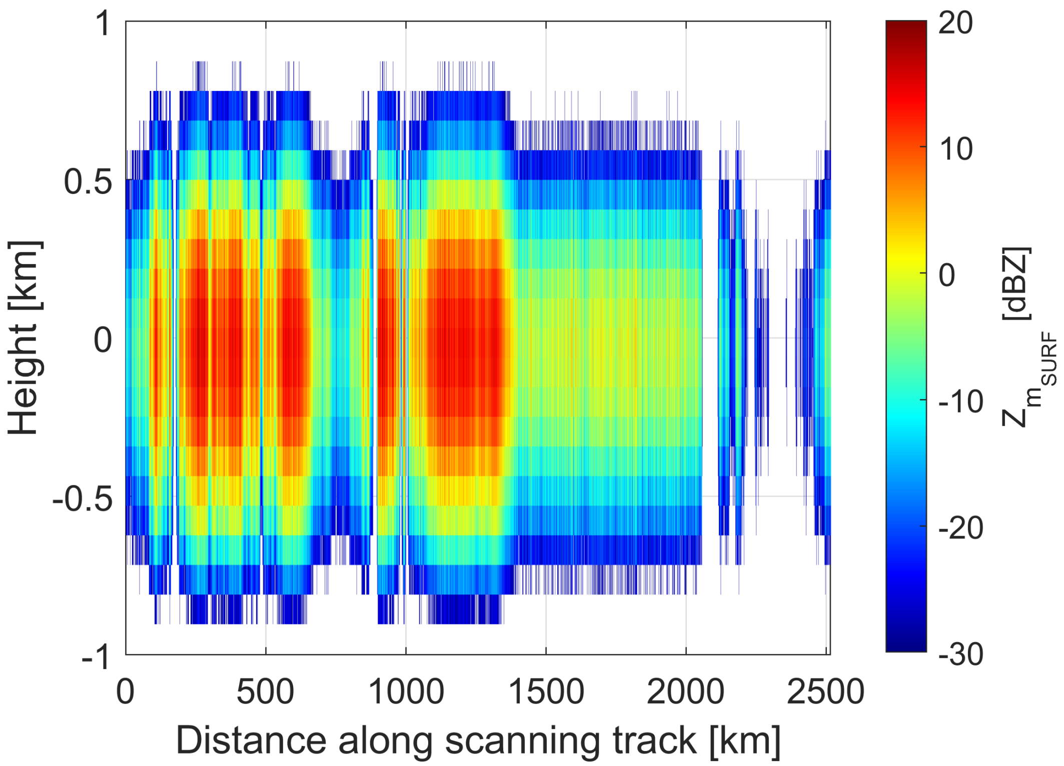

Figure 4.9: Surface reflectivities.

Figure (4.10) illustrates the Doppler velocities related to the surface reflectivities. The figure displays a characteristic pattern of positive and negative velocities depending on the altitude and the azimuth angle, while zero velocities at all altitudes are observed when the radar points at $\delta = 90°$ and $\delta = 270°$ with respect to the satellite velocity. Since the total Doppler velocity is a reflectivity weighted average of atmospheric and surface Doppler velocities (as shown in equation (3.43)), the bias caused by the surface will depend, other than azimuth and altitude, also on the relative strength of the echoes coming from the atmosphere and the surface.

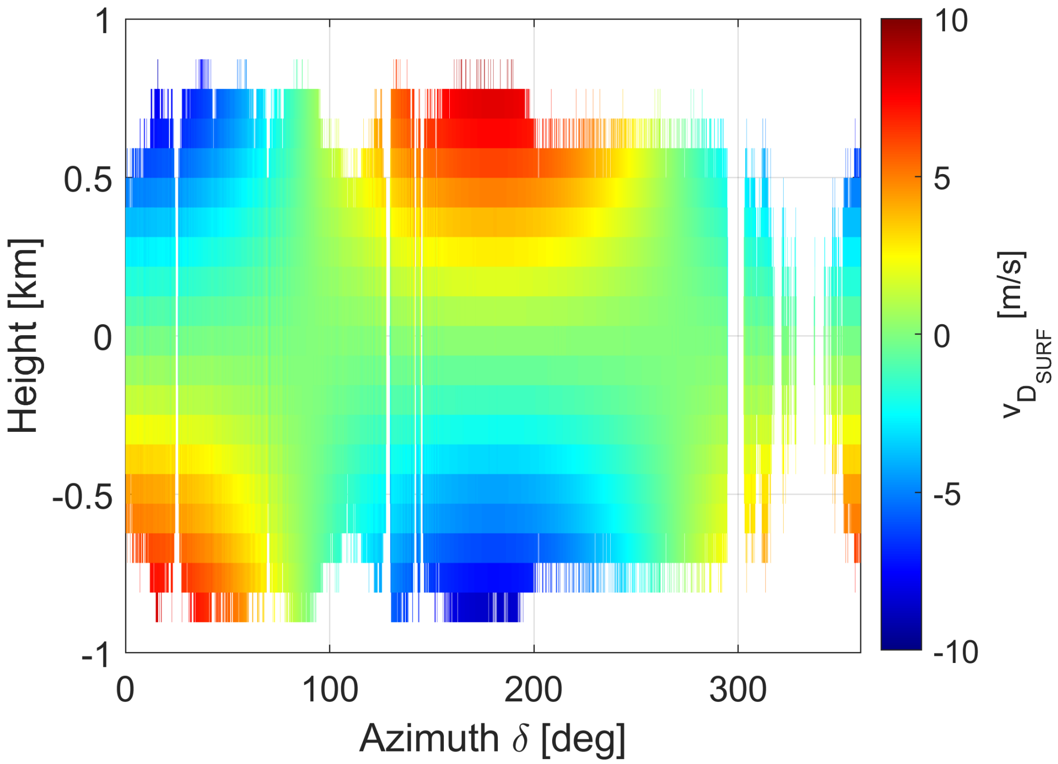

Figure 4.10: Doppler velocities of the surface.

At this point, the results presented separately for the surface and the atmosphere can be merged in single plots. Figure (4.11) shows the total reflectivities Z_{12} (eq. (3.47)), comprehensive of surface and atmospheric reflectivities, cross-talks between H and V channels and noise. The results represent an average of M= 8 pulse pairs, which lead to an increase in the radar sensitivity from $-18\,\mathrm{dB}Z$ (single pulse sensitivity) to $-22.5\,\mathrm{dB}Z$, allowing the detection of weaker echoes. The image displays only the reflectivities above the sensitivity level of $-22.5\,\mathrm{dB}Z$. Particularly evident is the strength of echoes from the land surfaces, which overshadows the atmospheric returns between ± 0.5 km. The surface also causes ghost echoes to appear at ± 2.3 km, leading to the erroneous detection of atmospheric targets where no real cloud is present. In particular, the ghosts at 2.3 km originating from land appear to be strong enough to bias the atmospheric returns at that height.

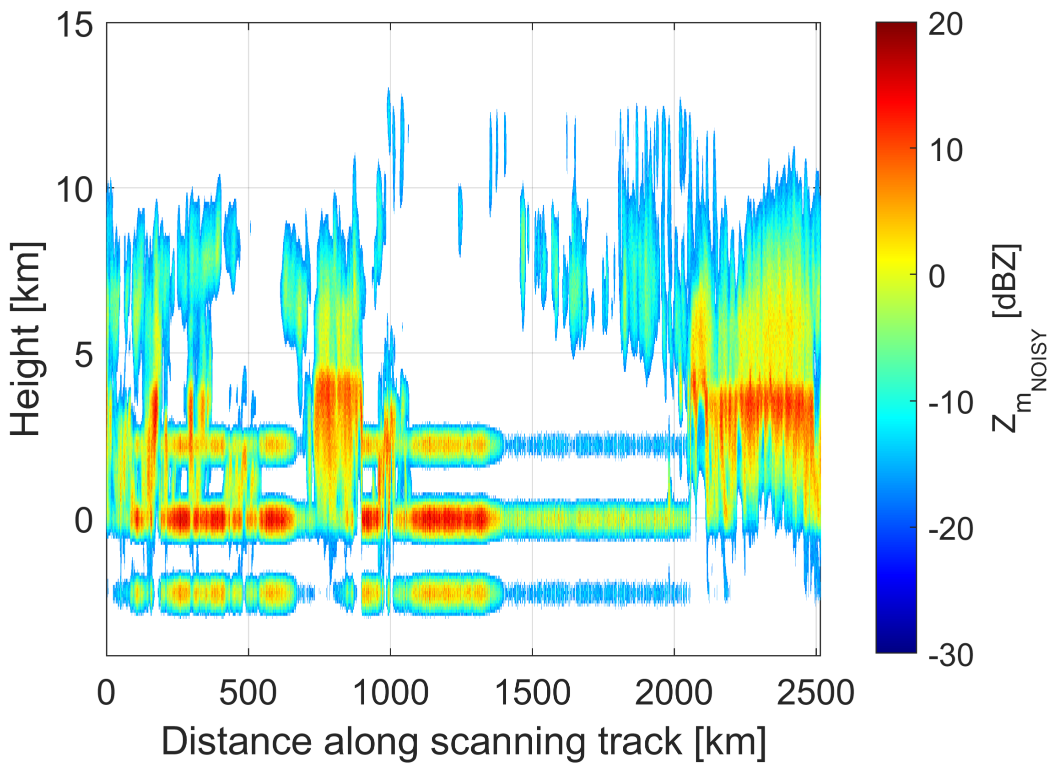

Figure 4.11: Total reflectivities with ghosts and noise.

Figure (4.12) illustrates the total Doppler velocities related to the reflectivities of figure (4.11). The image shows how the surface tends to bias the Doppler velocities of the atmospheric targets towards 0 m/s and the effect of ghost echoes. Since the phase of ghost echoes decorrelates between two pulses and is not correlated with the actual returns from targets, their presence will not produce any bias in Doppler velocities but only increase the random errors [16]. Notice how the regions with low Signal to Ghost ratios (figure (4.13)) or reflectivities near the noise level result indeed in a noisier Doppler estimate (corresponding to a more grainy texture in figure (4.12)).

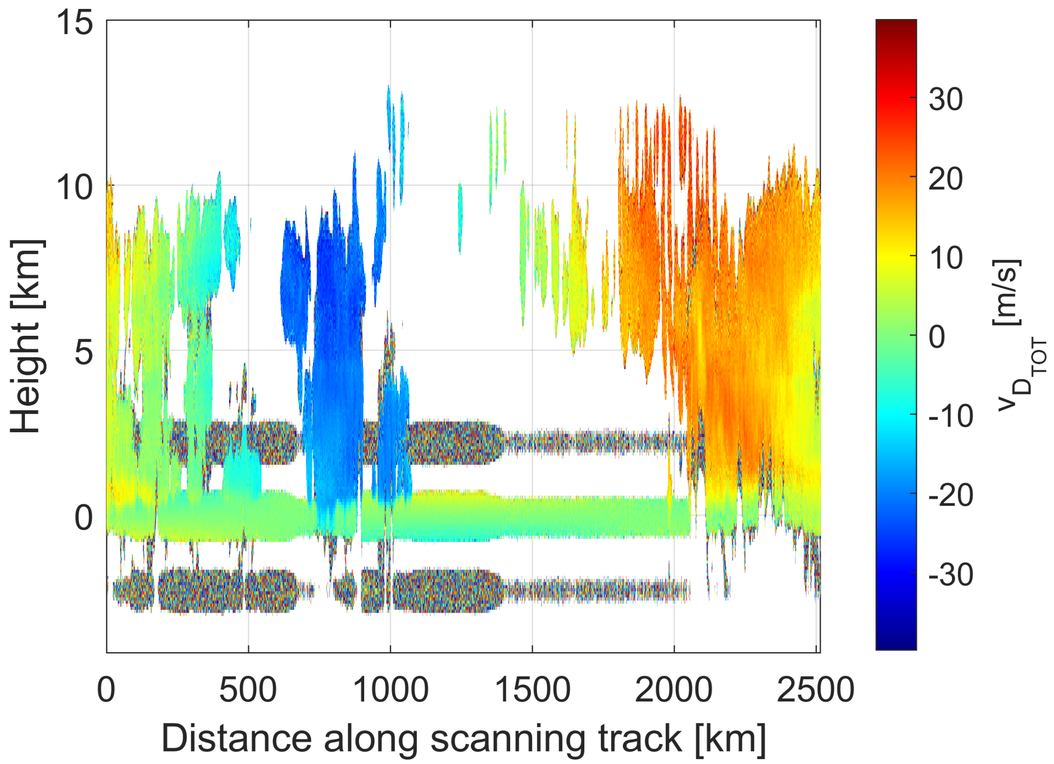

Figure 4.12: Total Doppler velocities with ghosts and noise.

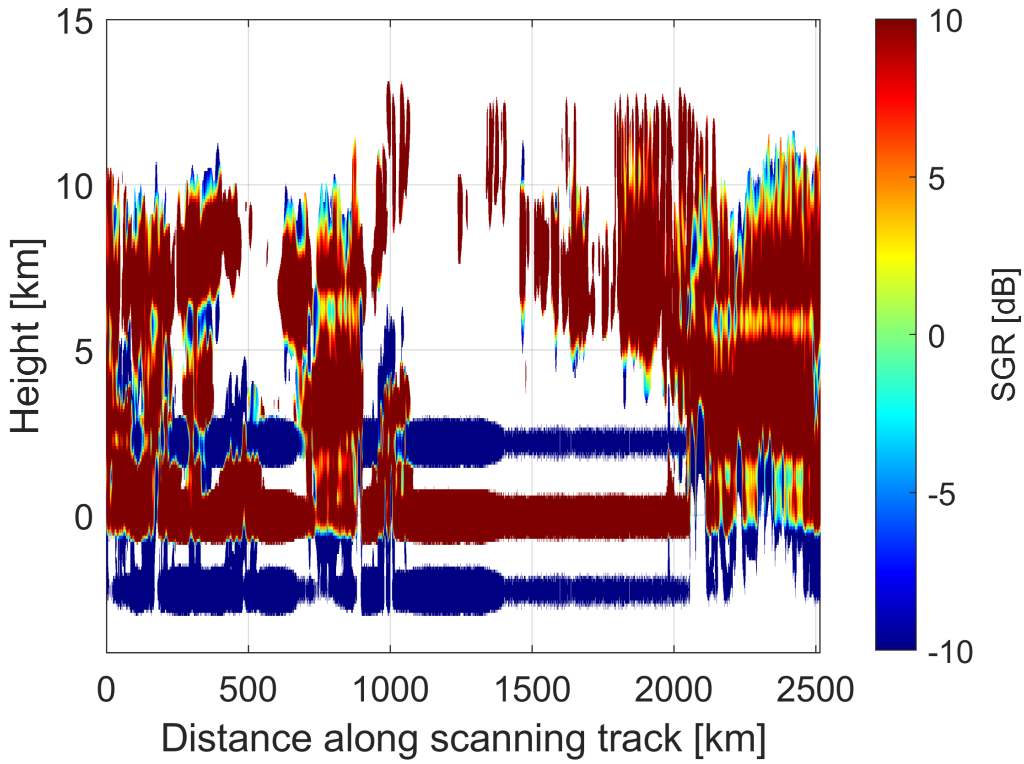

Figure 4.13: Signal to Ghost (SGR) ratio.

4.3 Wivern performance assessment

In addition to the computation and visualization of radar products, the simulator also represents a valuable tool to estimate the errors affecting the measurements. First of all, the Doppler velocities present a random noise depending on the strength of the echoes returned by the targets and the cross-talk between the two channels. In the simulator, the noise added to the Doppler velocities is computed from the variance defined in equation (2.22), which accounts for these two noise sources through the signal to noise (SNR) ratio and the signal to ghost (SGR) ratio. Other than random noises, there are additional disturbances such as mispointing, non-uniform beam filling and wind shear that lead to velocity biases on the Doppler measurements and hence must be considered.

The first error analyzed is the mispointing, which derives from an erroneous knowledge of the boresight direction. From the time series of figure (3.7), it is possible to determine the error affecting the azimuth angle over time. Figure (4.14) shows the values of $\Delta\delta_{mis}$ over the single scan considered for the simulation.

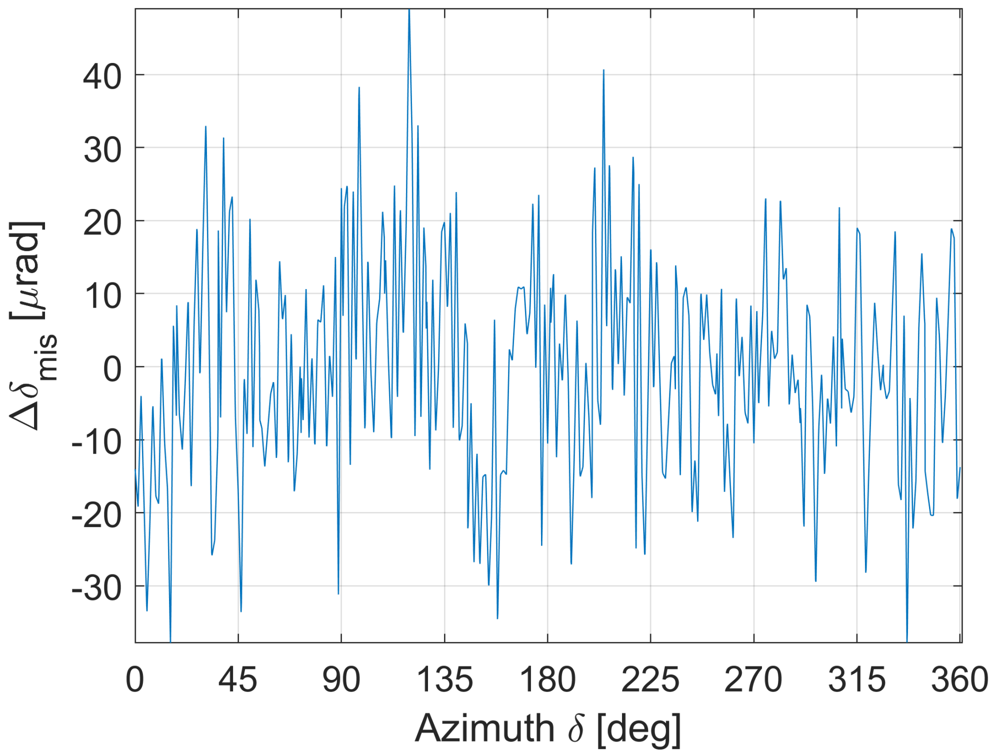

Figure 4.14: Azimuthal mispointing errors.

As reported in subsection (3.4.9), the values of $\Delta\delta_{mis}$ can be used to determine the mispointed boresight unit vector and hence, by employing equation (3.48), the mispointing error Δv_{mis}. The results illustrated in figure (4.15) shows that Δv_{mis} is a strong function of the azimuth angle, with the error maximized when the radar points perpendicularly to the satellite velocity ($\delta = 90°$, $\delta = 270°$), and minimized when pointing forward or backwards ($\delta = 0°$, $\delta = 180°$). In any case, figure (4.15) shows that the error due to azimuthal mispointing remains always smaller than $0.2\,\mathrm{m/s}$, thus it will provide a very small contribution to the Doppler velocity error budget.

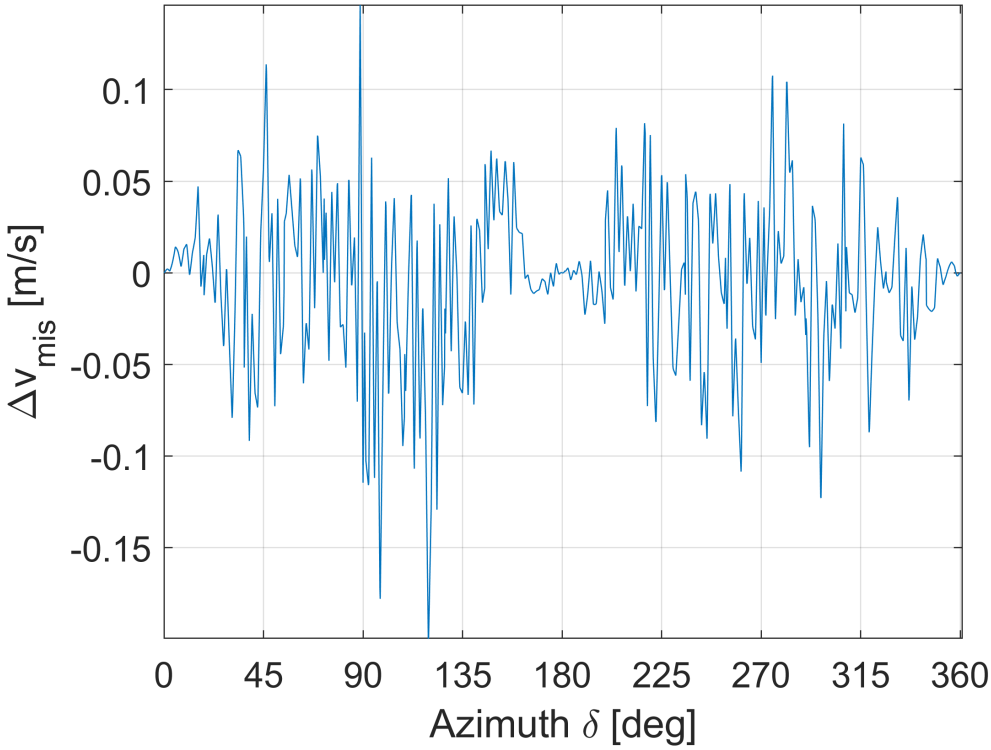

Figure 4.15: Mispointing errors on Doppler velocities.

The other sources of disturbances are the reflectivity gradient-based biases like non-uniform beam filling and wind shear. The wind shear errors (figure (4.16)) occur when reflectivity and velocity gradients are present at the same within the backscattering volume, as usually happens at the boundaries of clouds. In the current simulation, strong wind shears appear at near-surface altitudes (as illustrated in figure (4.7)), which result in significant errors (exceeding ± 1 m/s) affecting the measurements at the low altitudes. Nevertheless, figure (4.16) shows that these errors impact only limited regions and are close to zero for most areas within the observed scene.

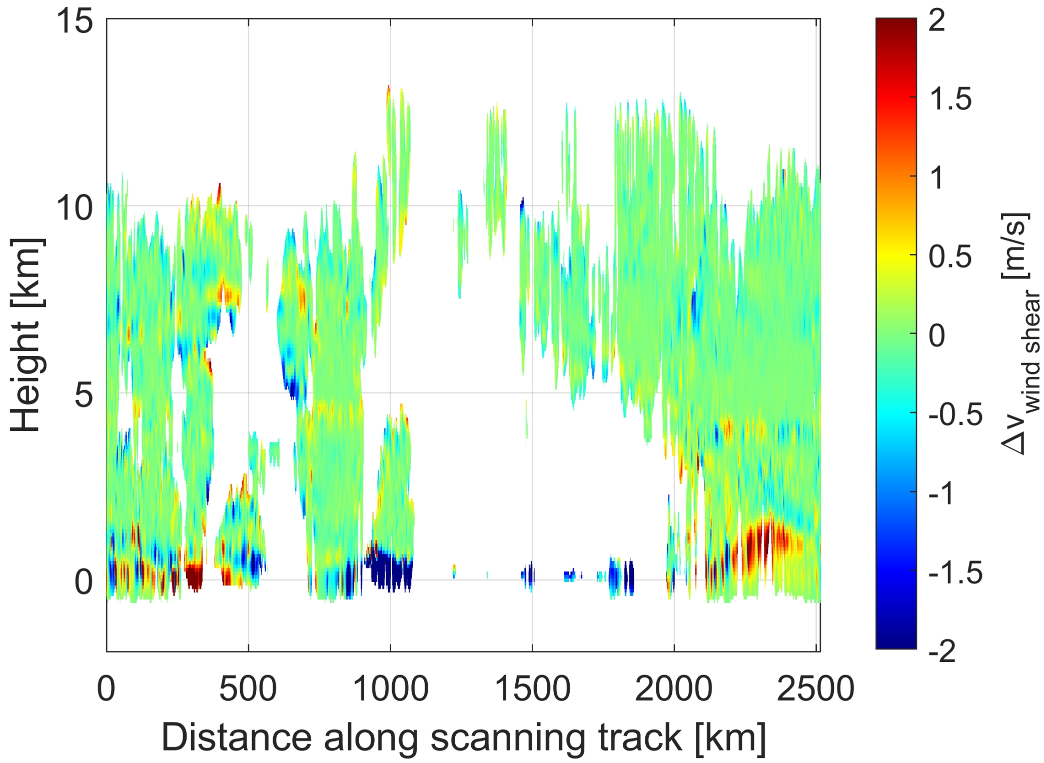

Figure 4.16: Errors induced by wind shear.

Lastly, there are biases due to non-uniform beam filling. For the cloud scene illustrated in figure (4.4), the distribution of the NUBF Doppler velocity biases as a function of the azimuthal scanning angle is shown in figure (4.17). The graph derives from a larger set of data obtained through a fictitious rotation of the satellite velocity vector at each instant of the single scan time discretization. As can be observed, the NUBF velocity bias appears to be maximum when the radar points in the forward and backward directions ($\delta = 0°$, $\delta = 180°$), and minimum when pointing side views ($\delta = 90°$, $\delta = 270°$). Even if the figure shows the presence of errors exceeding $\pm 5\,\mathrm{m/s}$, it must be noted that the occurrences is plotted on a logarithmic scale, which means that most of the biases occurring during the scan (yellow region) are nearly zero (because many NUBF errors are equal and opposite within the backscattering volume, so will tend to cancel out).

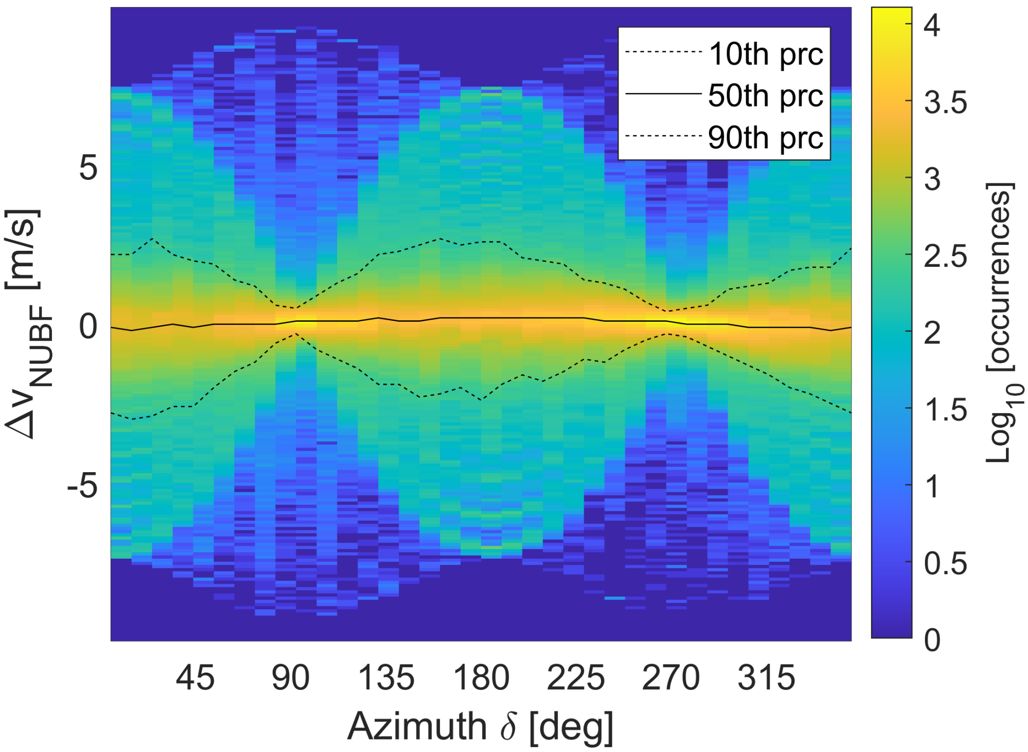

Figure 4.17: NUBF-induced errors as a function of the azimuthal scanning angle. The color modulates the log10 of the number of occurrences. The dotted lines represent the 10th and 90th percentile, whereas the continuous line corresponds to the median value.

Up to this point, different measurements biases have been analyzed individually. This procedure is quite helpful to understand the relative incidence of each disturbance to the error budget and identify the situations where they affect measurements the most. However, this approach doesn't show how these errors combine to generate the absolute error Δv_{tot} affecting the Doppler measurements. To determine the total error is possible to add the mispointing errors Δv_{mis} to the noisy Doppler velocities of figure (4.12) and then subtract the ideal LOS winds field of figure (4.7). The final result, shown in figure (4.18), is the total error Δv_{tot} inclusive of the noise and the mispointing, non-uniform beam filling and wind shear velocity biases. Ultimately, these results can be compared to the specifications reported in table (1.1) to assess the mission requirements. The 2 m/s accuracy requirement on horizontal winds (HLOS) corresponds roughly to 1.4 m/s on LOS winds, which is met for most areas of the observed scene. It should be noted that the results found derive from 1 km integration, when in fact, the winds can be averaged over a greater number of pulses (up to 20 km integration), thus leading to a reduction of the noise and consequentially to even better accuracies. In conclusion, the present simulation proved that requirements on wind accuracy are at reach.

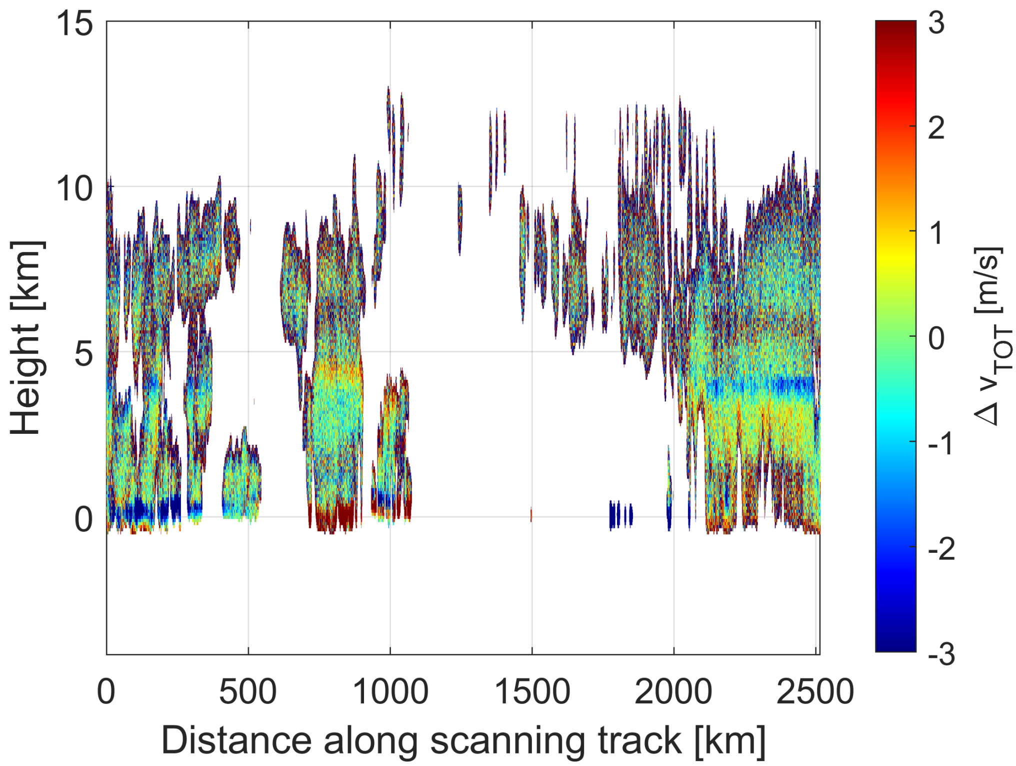

Figure 4.18: Total errors affecting the Doppler measurements within the observed scene.

Conclusions

This dissertation describes the development of an original cutting edge end-to-end simulator for a space-borne conically scanning Doppler radar adopting polarization diversity. The simulator primarily implements an orbital propagator, the scanning geometry and the radar illumination, coupled with a global atmospheric circulation model providing fine resolution vertical profiles of winds and clouds. The coupling between the orbit and the atmospheric model allows global scale simulations of mission observables, i.e. reflectivities and Doppler velocities of atmospheric targets. In addition, a surface modelling has been carried out to characterize the unwanted returns from land and sea surfaces. The simulator also implements the errors on Doppler measurements, such as intrinsic noise, cross-talk noise between the two diversely polarized channels and velocities biases due to reflectivity gradients (i.e., wind shear and non-uniform beam filling). Additional disturbances originate from the antenna azimuthal mispointing errors, represented in the form of an absolute knowledge error power spectrum, later converted to a time series.

The characterization of the errors and the isolation of each single error source makes the simulator a perfect tool to verify mission performances and compliance with requirements, which will be part of the Phase 0 studies beginning in December 2021. Moreover, the end-to-end simulator will be exploited to determine the main source of errors and perform the consequent trade-offs between radar configurations in order to minimize their contribution to the total error. Preliminary findings show that mispointing errors associated to the antenna azimuthal mispointing are expected to be lower than 0.3 m/s (and strongly dependent on the antenna azimuthal scanning angle), wind shear and non-uniform beam filling errors have negligible biases (with the latter presenting random errors strongly dependent on the antenna azimuthal scanning angle but typically lower than 1 m/s), and cross-talk effects are well predictable so that areas affected by strong cross-talk noise can be flagged. The noise random errors are dependent on the SNR and the possible presence of ghosts (which can be flagged); they can be be reduced by averaging over a higher number of pulses (i.e. by using a longer integration time). From preliminary simulations the quality of the Doppler appears to strongly depend on several factors: the strength of the cloud reflectivity, the antenna pointing direction relative to the satellite motion, the presence of strong reflectivity and/or wind gradients, the strength of the surface clutter. Overall, the total wind errors seem to meet the mission requirements in a good portion of the clouds detected by the WIVERN radar, which is a very encouraging result at the beginning of Phase 0 studies. The results of this thesis have contributed to the main results of a paper under submission for the EGU Atmospheric Measurement Technique journal [8].

Future work

The E2E simulator described here represents a preliminary version of the complete tool that will be used during Wivern phase 0 studies and beyond. The first improvements may involve a more accurate orbital model and a more detailed Earth modelling. More sophisticated surface modelling could be introduced by including the dependence on the surface winds over the ocean and different surface types/orography over land. Similarly, a more accurate atmospheric model can be used at a regional or even global scale with cloud scenes characterized by a finer horizontal resolution ($< 1\,\text{km}$). Further modifications will certainly concern the radar, starting from the pulse shape and substituting the Gaussian antenna pattern with a more realistic one comprehensive of sidelobes. Lastly, the attitude model of a satellite with a rotating antenna can be introduced in the simulator to provide a better characterization of the pointing.

Appendix A

Transformations and rotations

A.1 Transformation matrices

In three dimensions, any coordinate transformation can be expressed by the product of the three elementary matrices, defined as follows:

$$\mathbf{L}_1(\phi) = \begin{bmatrix} 1 & 0 & 0 \\ 0 & \cos\phi & -\sin\phi \\ 0 & \sin\phi & \cos\phi \end{bmatrix} \tag{A.1}$$

$$\mathbf{L}_2(\theta) = \begin{bmatrix} \cos\theta & 0 & \sin\theta \\ 0 & 1 & 0 \\ -\sin\theta & 0 & \cos\theta \end{bmatrix} \tag{A.2}$$

$$\mathbf{L}_3(\psi) = \begin{bmatrix} \cos\psi & -\sin\psi & 0 \\ \sin\psi & \cos\psi & 0 \\ 0 & 0 & 1 \end{bmatrix} \tag{A.3}$$

Being ϕ, θ and ψ three generic rotation angles about the x, y, and z axes, respectively. The coordinate transformation from the perifocal reference frame (pqw) to the geocentric equatorial reference frame (IJK) is then given by:

$$\mathbf{L}_{PI} = \mathbf{L}_3(\Omega)\mathbf{L}_1(i)\mathbf{L}_3(\omega) \tag{A.4}$$

where Ω is the RAAN, i is the inclination and ω is the argument of perigee. If the Local-Vertical-Local-Horizontal (LVLH) reference frame is defined as in section (3.2), then the transformation matrix from LVLH to IJK is given by:

$$\mathbf{L}_{LI} = \mathbf{L}_3(\Omega)\mathbf{L}_1(i)\mathbf{L}_3(\omega + \nu) \tag{A.5}$$

being ν the true anomaly.

Among the coordinates transformations carried out, there are the ones concerning topocentric reference frames. The transformation matrix from the South-East-Zenith (SEZ) reference frame to IJK is:

$$\mathbf{L}_{SI} = \begin{bmatrix} \cos\alpha & -\sin\alpha & 0 \\ \sin\alpha & \cos\alpha & 0 \\ 0 & 0 & 1 \end{bmatrix} \begin{bmatrix} \sin\delta_d & 0 & \cos\delta_d \\ 0 & 1 & 0 \\ -\cos\delta_d & 0 & \sin\delta_d \end{bmatrix} \tag{A.6}$$

where α is the right ascension (measured from the axis $\hat{I}$ of the IJK reference frame) of the point in which the topocentric reference frame is centered, while δ_d is its declination (corresponding to the latitude La). Lastly, there is the modified SEZ reference frame introduced in subsection (3.3.2). The projection of the boresight vector $\vec{s}_{h0\,SEZ} = \mathbf{L}_{SI}^T \vec{s}_{h0\,IJK}$ on the tangent plane (figure 3.9) is simply given by $\vec{s}_{h0_\perp\,SEZ} = \{x_{SEZ},\, y_{SEZ},\, 0\}$, which forms and angle ξ with the unit vector $\hat{S}_{SEZ} = \{1,\, 0,\, 0\}$ (the x-axis of the SEZ frame). The rotation of ξ about the $\hat{Z}$ axis generate the modified topocentric reference frame $(\hat{T}_1\hat{T}_2\hat{Z})$, with the coordinate transformation matrix from this reference frame to IJK given by:

$$\mathbf{L}_{TI} = \mathbf{L}_{SI}\mathbf{L}_3(\xi) \tag{A.7}$$

A.2 Quaternions

The rotation of a generic vector $\vec{v}$ around an axis can be described by the *quaternion* operator, which is defined as:

$$\mathfrak{q} = \left\{\cos\left(\frac{\alpha}{2}\right), u_1\sin\left(\frac{\alpha}{2}\right), u_2\sin\left(\frac{\alpha}{2}\right), u_3\sin\left(\frac{\alpha}{2}\right)\right\} \tag{A.8}$$

Where $\hat{u} = \{u_1, u_2, u_3\}$ is the generic unit vector identifying the rotation axis direction and α is the angle of rotation about the axis. The quaternion can be associated to a rotation matrix by the following relation:

$$\mathbf{T}(\mathfrak{q}) = \begin{bmatrix} q_0^2+q_1^2-q_2^2-q_3^2 & 2(q_1q_2-q_0q_3) & 2(q_1q_3+q_0q_2) \\ 2(q_1q_2+q_0q_3) & q_0^2-q_1^2+q_2^2-q_3^2 & 2(q_2q_3-q_0q_1) \\ 2(q_1q_3-q_0q_2) & 2(q_2q_3+q_0q_1) & q_0^2-q_1^2-q_2^2+q_3^2 \end{bmatrix} \tag{A.9}$$

Thus the rotated vector $\vec{v}_{rot}$ can be obtained by:

$$\vec{v}_{rot} = \mathbf{T}(\mathfrak{q})\vec{v} \tag{A.10}$$

Bibliography

[1] European Space Agency. *About Earth Explorers*. URL: https://www.esa.int/Applications/Observing_the_Earth/Future_EO/Earth_Explorers/About_Earth_Explorers2 (cit. on p. 2).

[2] European Space Agency. *Aeolus Overview*. URL: https://earth.esa.int/eogateway/missions/aeolus/description (cit. on p. 2).

[3] European Space Agency. *Four mission ideas to compete for Earth Explorer 11*. URL: https://www.esa.int/Applications/Observing_the_Earth/Future_EO/Earth_Explorers/Four_mission_ideas_to_compete_for_Earth_Explorer_11 (cit. on p. 2).

[4] European Space Agency. *Measuring winds*. URL: https://www.esa.int/Applications/Observing_the_Earth/Aeolus/Measuring_wind (cit. on pp. 1, 2).

[5] Clive Alabaster. *Pulse Doppler Radar: Principles, Technology, Applications*. SciTech Publishing, 2012 (cit. on pp. 10, 12).

[6] Roger R. Bate, Donald D. Mueller, and Jerry E. White. *Fundamentals of Astrodynamics*. Dover Publications, 1971 (cit. on p. 23).

[7] A. Battaglia, R. Dhillon, and A. Illingworth. «Doppler W-band polarization diversity space-borne radar simulator for wind studies». In: *Atmospheric Measurement Techniques* 11.11 (2018), pp. 5965–5979. DOI: 10.5194/amt-11-5965-2018 (cit. on pp. 19, 42).

[8] A. Battaglia, Martire P., Caubet E., Phalippou L., Stesina F., Kollias P., and A. Illingworth. «End to end simulator for the WIVERN W-band Doppler conically scanning spaceborne radar to provide global observations of in-cloud winds and hydrometeor characteristics». In: (2021). submitted (cit. on p. 63).

[9] A. Battaglia, M. Wolde, L.P. D'Adderio, C. Nguyen, F. Fois, A. Illingworth, and R. Midthassel. «Characterization of Surface Radar Cross Sections at W-Band at Moderate Incidence Angles». In: *IEEE Transactions on Geoscience and Remote Sensing* 55.7 (2017), pp. 3846–3859. DOI: 10.1109/TGRS.2017.2682423 (cit. on p. 36).

[10] Alessandro Battaglia and Pavlos Kollias. «Error Analysis of a Conceptual Cloud Doppler Stereoradar with Polarization Diversity for Better Understanding Space Applications». In: 32.7 (2015), pp. 1298–1319. DOI: `10.1175/JTECH-D-14-00015.1`. eprint: `https://doi.org/10.1175/JTECH-D-14-00015.1`. URL: `https://doi.org/10.1175/JTECH-D-14-00015.1` (cit. on pp. 12, 13).

[11] Alessandro Battaglia, Pavlos Kollias, Ranvir Dhillon, Richard Roy, Simone Tanelli, Katia Lamer, Mircea Grecu, Matthew Lebsock, Daniel Watters, Kamil Mroz, Gerald Heymsfield, Lihua Li, and Kinji Furukawa. «Spaceborne Cloud and Precipitation Radars: Status, Challenges, and Ways Forward». In: *Reviews of Geophysics* 58.3 (2020). e2019RG000686 10.1029/2019RG000686, e2019RG000686. DOI: `10.1029/2019RG000686`. eprint: `https://agupubs.onlinelibrary.wiley.com/doi/pdf/10.1029/2019RG000686`. URL: `https://agupubs.onlinelibrary.wiley.com/doi/abs/10.1029/2019RG000686` (cit. on p. 9).

[12] Alessandro Battaglia, Simone Tanelli, and Pavlos Kollias. «Polarization Diversity for Millimeter Spaceborne Doppler Radars: An Answer for Observing Deep Convection?» In: *Journal of Atmospheric and Oceanic Technology* 30.12 (2013), pp. 2768–2787. DOI: `10.1175/JTECH-D-13-00085.1` (cit. on pp. 13, 42).

[13] Michel Capderou. *Handbook of Satellite Orbits*. Springer International Publishing, 2014 (cit. on pp. 21, 22).

[14] Howard D. Curtis. *Orbital Mechanics for Engineering Students*. Butterworth-Heinemann, 2019 (cit. on pp. 21–23).

[15] Frédéric Fabry. *Radar Meteorology*. Cambridge University Press, 2015 (cit. on pp. 7–10, 12, 13, 16).

[16] A.J. Illingworth, A. Battaglia, J. Bradford, M. Forsythe, P. Joe, P. Kollias, K. Lean, M. Lori, J.F. Mahfouf, S. Melo, R. Midthassel, Y. Munro, J. Nicol, R. Potthast, M. Rennie, T.H.M. Stein, S. Tanelli, F. Tridon, C.J. Walden, and M. Wolde. «WIVERN: A New Satellite Concept to Provide Global In-Cloud Winds, Precipitation, and Cloud Properties». In: *Bulletin of the American Meteorological Society* 99.8 (Aug. 2018), pp. 1669–1687. DOI: `10.1175/BAMS-D-16-0047.1` (cit. on pp. 1, 4, 14, 16, 17, 42, 55).

[17] A.J. Illingworth, A. Battaglia, J. Delanoe, G. Halloran, P. Kollias, S. Laroche, J.F. Mahfouf, R. Potthast, M. Rennie, C.J. Walden, and M. Wolde. *WIVERN: A WInd VElocity Radar Nephoscope for observing global winds, clouds and precipitation*. A proposal submitted to ESA in response to the Call for Earth Explorer-11 Mission Ideas. Dec. 2020 (cit. on pp. 2–6, 18, 20, 27).

[18] R. Jeffrey Keeler and Richard E. Passarelli. «Signal Processing for Atmospheric Radars». In: *Radar in Meteorology: Battan Memorial and 40th Anniversary Radar Meteorology Conference*. Ed. by David Atlas. Boston, MA: American Meteorological Society, 1990, pp. 199–229. DOI: `10.1007/978-1-935704-15-7_21` (cit. on p. 12).

[19] P. Mazzoldi, M. Nigro, and C. Voci. *Fisica Vol. II - Elettromagnetismo e onde*. EdiSES, 1998 (cit. on p. 13).

[20] Robert Meneghini and Toshiaki Kozu. *Spaceborne weather radar*. Artech House, 1990 (cit. on p. 4).

[21] World Meteorological Organization. *WMO strategic plan 2020–2023*. 2019 (cit. on p. 1).

[22] Andrew L. Pazmany, John C. Galloway, James B. Mead, Ivan Popstefanija, Robert E. McIntosh, and Howard W. Bluestein. «Polarization Diversity Pulse-Pair Technique for Millimeter-Wave Doppler Radar Measurements of Severe Storm Features». In: *JAOT* 16.12 (1999), pp. 1900–1911. DOI: `10.1175/1520-0426(1999)016<1900:PDPPTF>2.0.CO;2` (cit. on pp. 13, 18, 42).

[23] W.H. Press, S.A. Teukolsky, W.T. Vetterling, and B.P. Flannery. *Numerical Recipes in C*. Cambridge University Press, 1992 (cit. on p. 29).

[24] Martin Schetzen. *Airborne Doppler Radar: Applications,Theory, and Philosophy*. American Institute of Aeronautics and Astronautics, Inc., 2006 (cit. on p. 12).

[25] S. Tanelli, E. Im, S. L. Durden, L. Facheris, D. Giuli, and E.A. Smith. «Rainfall Doppler velocity measurements from spaceborne radar: overcoming nonuniform beam filling effects». In: 21.1 (2004). doi: 10.1175/1520-0426, pp. 27–44 (cit. on pp. 12, 18).

[26] M. Wolde, A. Battaglia, C. Nguyen, A. L. Pazmany, and A. Illingworth. «Implementation of polarization diversity pulse-pair technique using airborne W-band radar». In: 12.1 (2019), pp. 253–269. DOI: `10.5194/amt-12-253-2019`. URL: `https://www.atmos-meas-tech.net/12/253/2019/` (cit. on p. 13).

[27] Guifu Zhang. *Weather Radar Polarimetry*. CRC Press, 2017 (cit. on p. 16).